Anisotropic electron-hole excitation and large linear dichroism in the two-dimensional ferromagnet CrSBr with in-plane magnetization

Tian-Xiang Qian,[1,2] Ju Zhou ●,[1,3] Tian-Yi Cai,[1,*] and Sheng Ju[1,4,†]

[1]*School of Physical Science and Technology and Jiangsu Key Laboratory of Thin Film, Soochow University, Suzhou 215006, People's Republic of China*
[2]*Dipartimento di Fisica, Università degli Studi di Milano, via Celoria 16, I-20133 Milano, Italy*
[3]*School of Mathematics and Physics, Queen's University Belfast, Belfast BT7 1NN, Northern Ireland, United Kingdom*
[4]*School of Optical and Electronic Information, Suzhou City University, Suzhou 215104, People's Republic of China*

The observation of magnetic ordering in atomically thin CrI_3 and $Cr_2Ge_2Te_6$ monolayers has aroused intense interest in condensed-matter physics and material science. Studies of van de Waals two-dimensional (2D) magnetic materials are of both fundamental importance and application interest. In particular, exciton-enhanced magneto-optical properties revealed in CrI_3 and $CrBr_3$ monolayers have expanded the understanding of exciton physics in 2D materials. Unlike CrI_3 and $CrBr_3$, with out-of-plane magnetization, CrSBr has an in-plane magnetic moment, therefore providing a good opportunity to study the magnetic linear dichroism and high-order magneto-optical effects. Here, based on the many-body perturbation method within density-functional theory, we have studied quasiparticle electronic structure, exciton, and optical properties in CrSBr monolayer. A strongly bounded exciton has been identified with the first bright exciton located at 1.35 eV, in good agreement with an experiment of photoluminescence [Wilson *et al.*, Nat. Mater. **20**, 1657 (2021)]. Strong contrast in the optical absorption is found between the electric fields lying along the in-plane two orthogonal directions. In accordance with a typical and realistic experimental setup, we show that the rotation angle of linear polarized light, either reflected or transmitted, could be comparable with those revealed in black phosphorene. Such large linear dichroism arises mainly from the anisotropic in-plane crystal structure. The magnetic contribution from the off-diagonal component of dielectric function to the linear dichroism in CrSBr is negligible. Our findings not only have revealed the excitonic effect on the optical and magneto-optical properties in 2D ferromagnet CrSBr, but also have shown its potential applications in 2D optics and optoelectronics.

I. INTRODUCTION

Due to strong light-matter interaction, two-dimensional (2D) materials have demonstrated potential applications in semiconductor optoelectronics and photonics [1–4]. The discovery of 2D van der Waals magnets $Cr_2Ge_2Te_6$ [5] and CrI_3 [6] monolayer, on the other hand, has provided an additional degree of freedom, where the out-of-plane magnetization could facilitate magneto-optical Kerr and Faraday effects in the ultrathin limit [7,8]. Based on many-body perturbation theory, Wu *et al.* have revealed the exciton effect on the magneto-optical effects in the monolayer of CrI_3 [9] and $CrBr_3$ [10]. The Kerr rotation angle for the reflected light could reach as high as $0.9°$, and the Faraday angle for the transmitted light could reach as high as $0.3°$. Recently, another kind of 2D magnet, CrSBr, with in-plane magnetization has been identified [11] and fabricated [12]

successfully. The bilayer system shows great contrast in the optical responses between antiferromagnetic and ferromagnetic interlayer coupling [12]. Considering the excitonic effect, such as a magnetic ordering dependence of optical properties, has been well explained by the many-body perturbation calculations [12]. In the monolayer limit, the system shows strong photoluminescence (PL) at 1.3 eV [12]. In the meantime, the exciton-coupled coherent magnons will lead to efficient optical access to spin information [13]. In contrast to $Cr_2Ge_2Te_6$ and CrI_3 ($CrBr_3$), when the magnetization in CrSBr monolayer is lying along the easy axis within the 2D plane, as demonstrated in Fig. 1, the former magneto-optical Kerr and Faraday effects, which measure the rotation angle of linear polarized light, will be replaced by the Schäfer-Hubert (SH) effect and Voigt effect for reflected and transmitted lights, respectively [14]. The original purpose of this paper is to provide a comprehensive framework of the excitonic effect on the optical and high-order magneto-optical properties in 2D ferromagnetic CrSBr with in-plane magnetization. Generally, when the magnetization is pointing along the *y* direction, it is believed that [14]

$$\phi_{SH} = \theta_{SH} + i\eta_{SH} = \frac{-i\omega d}{c(1 - n_{sub}^2)}(n_\parallel^2 - n_\perp^2)$$

$$= \frac{-i\omega d}{c(1 - n_{sub}^2)}\left(\varepsilon_{yy} - \varepsilon_{xx} - \frac{\varepsilon_{zx}^2}{\varepsilon_{zz}}\right), \quad (1)$$

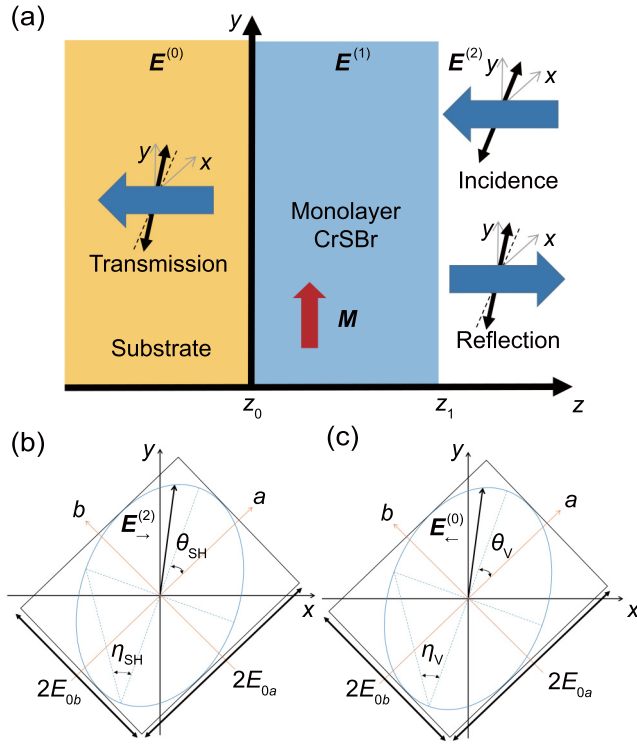*caitianyi@suda.edu.cn
†jusheng@suda.edu.cn

FIG. 1. Schäfer-Hubert (SH) and Voigt setup consisting of layers of vacuum, ferromagnetic monolayer CrSBr, and a substrate of semi-infinitely thick α-Al$_2$O$_3$. Red arrow denotes the in-plane magnetization, which is along the y axis. (b) Illustration of rotation angle and ellipticity for reflected (left panel) and transmitted (right panel) lights.

and

$$\phi_{\mathrm{V}} = \theta_{\mathrm{V}} - i\eta_{\mathrm{V}} = \frac{\omega d}{2ic}(n_{\parallel} - n_{\perp})$$

$$= \frac{\omega d}{2ic}\left[\varepsilon_{yy}^{\frac{1}{2}} - \left(\varepsilon_{xx} + \frac{\varepsilon_{zx}^2}{\varepsilon_{zz}}\right)^{\frac{1}{2}}\right]. \quad (2)$$

Here θ_{SH} and θ_{V} are rotation angles, and η_{SH} and η_{V} are ellipticities. c is the velocity of light, n is the complex refraction index, and ε is the dielectric function. ω is the optical frequency, d is the thickness of magnetic material, and sub means the substrate. Clearly, such effects are closely related to the contrast between the dielectric properties of two in-plane diagonal components ε_{xx} and ε_{yy} as well as the magnitude of the off-diagonal component ε_{zx} of the system of interest. Based on independent particle approximation (IPA), such effects in 2D magnets CrXY ($X = $ S, Se, and Te; $Y = $ Cl, Br, and I) were studied computationally [15]. For the monolayer geometry with particular 2D dielectric screening, the inherent many-body correction to the quasiparticle band structure and optical properties could not be ignored [16–21]. A huge excitonic effect with binding energy of as large as 1 eV (two orders larger than conventional semiconductors) will modify the optical spectrum from IPA strongly. Therefore, in this paper, based on density functional theory with many-body perturbation method, i.e., GW-BSE method (G for one-particle Green's function, W for screened Coulomb interaction, and BSE for Bethe-Salpeter equation)

[22], we have studied the quasiparticle electronic structure, exciton, and optical properties in CrSBr monolayer. The first bright excitonic state is found located at 1.35 eV, in good agreement with experiment [12]. In the meantime, a large linear dichroism (optical birefringence) from the anisotropic in-plane crystal structure has been identified. The intrinsic magneto-optical effect from the off-diagonal components of the dielectric function, however, is found to be very small. CrSBr shows a large difference between ε_{xx} and ε_{yy} which will dominate the linear dichroism and, consequently, the magnitude of rotation angle θ and ellipticity η. It has also been revealed that the excitonic effect has modified ε_{xx}, ε_{yy}, and ε_{xz} dramatically, and consequently, the linear dichroism and the high-order magneto-optical properties. When the magnetization is tuned by the external perpendicular magnetic field toward the out-of-plane direction, the CrSBr monolayer could exhibit significant Kerr and Faraday effects, which are even larger than those in CrI$_3$ [9] and CrBr$_3$ [10]. Furthermore, the short lifetime of the first bright exciton suggests its potential application in infrared light emission. Our findings not only have revealed the excitonic effect on the optical and magneto-optical properties in 2D ferromagnet CrSBr but also have shown its potential applications in 2D optics and optoelectronics.

II. COMPUTATIONAL METHOD

Our first-principles calculations are performed using density-functional theory (DFT) as implemented in the QUANTUM ESPRESSO package [23]. We use the generalized gradient approximation with Perdew-Burke-Ernzerhof (PBE) [24] and norm-conserving pseudopotentials with a plane-wave cutoff of 80 Ry [25]. The ground-state wave functions and eigenvalues are calculated within a k grid of 16×12×1. The structures are relaxed until the total forces are less than 0.01 eV/Å, and the convergence criterion for total energies is set to 10^{-5} eV. The quasiparticle band structure and excitonic properties are calculated with the BERKELEYGW package [26–29] (see Appendix A). We have included spin-orbit coupling with spinor GW-BSE calculations [29]. A slab model is used with vacuum layer of 15 Å along the out-of-plane direction, and a truncated Coulomb interaction between CrSBr monolayer and its periodic image is adopted [30]. Here the calculations are based on one-shot G_0W_0 with generalized plasmon pole model. The mean-field wave functions and eigenvalues within PBE are chosen as the starting point for G_0W_0, as a first guess for quasiparticle wave functions and eigenvalues. For the convergence of quasiparticle energies [31], we have tested the dependence on k-grid size, number of bands, as well as dielectric cutoff. We use a coarse k grid of 16×12×1, 1080 of number of bands, and a dielectric cutoff of 20 Ry (see Appendix B). The electron-hole excitations are then calculated by solving the BSE for each exciton state and frequency-dependent complex dielectric function $\varepsilon(\omega)$. For the BSE part, the fine k grid of 64×48×1 is used (see Appendix B). We use a Gaussian smearing with a broadening constant of 30 meV in the optical absorbance spectrum. The number of bands for optical transitions is six valence and eight conduction bands, which is sufficient to cover the span of the energies of visible light. Such treatment of excited states is
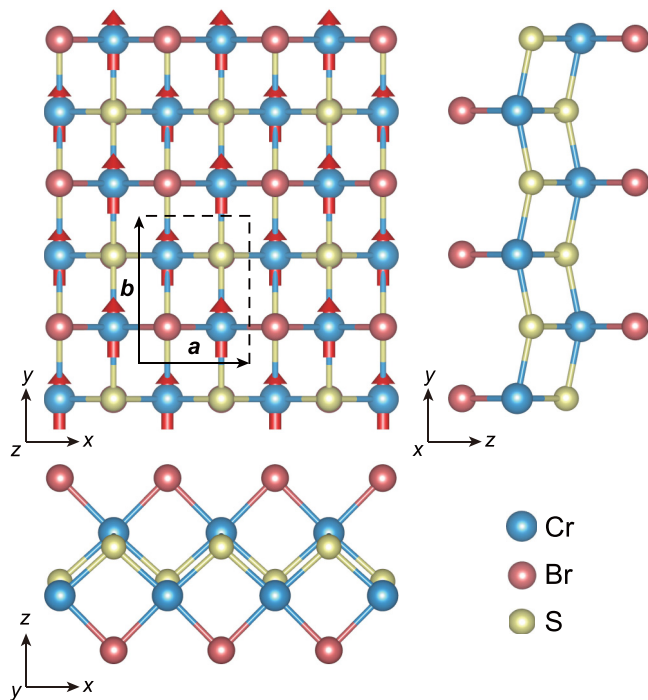
FIG. 2. Illustration of crystal structure of 2D magnet CrSBr monolayer. Local magnetic moment at Cr atoms pointing along y axis.

robust and has been applied successfully in a wide range of 2D materials [32], including graphene [33–39], graphyne [40], 2D transition-metal dichalcogenides [41–51], black phosphorene [52–56], blue phosphorene [57,58], violet (Hittorf's) phosphorene [59,60], 2D monochalcogenides [61–63], 2D GaN [64], 2D boron nitrides [65–67], and 2D magnets [9,10,68].

III. RESULTS AND DISCUSSION

Bulk CrSBr belongs to an orthorhombic structure with crystal parameters $a = 3.504$ Å, $b = 4.738$ Å, and $c = 7.907$ Å in the space group *Pmmn* (No. 59). This structure is built of monolayers of CrSBr, which are bonded through van der Waals interactions along the c axis. For monolayer CrSBr as demonstrated in Fig. 2, it still belongs to space group *Pmmn* (No. 59) with an effective thickness of around 5.7 Å. The monolayer CrSBr consists of two buckled rectangular planes of CrS fused together, with both surfaces capped by Br atoms. The top view of monolayer CrSBr in Fig. 2 shows a rectangular network lattice with $a = 3.537$ Å and $b = 4.730$ Å.

Experimentally, using a second-harmonic generation technique, ferromagnetic order with the magnetic moment pointing along the y axis has been identified in CrSBr monolayer with a Curie temperature of $T_C = 146 \pm 2$ K [69]. In the meanwhile, photoluminescence spectra show an obvious decrease at temperatures between 130 and 150 K, suggesting a phase transition therein [12]. This Curie temperature in CrSBr monolayer is therefore much higher than $Cr_2Ge_2Te_6$ monolayer (at 22 K under magnetic field of 0.075 T) [5] and CrI_3 monolayer (at 45 K) [6]. Theoretically, Cr^{3+} ion has a magnetic moment of 3 μ_B, pointing along the y axis of the 2D
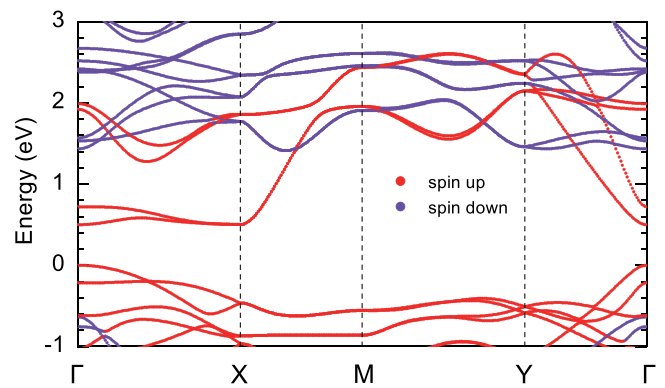

FIG. 3. PBE band structure with colors denoting the direction of spin polarization along the y axis.

plane. When the magnetization points along the x or z axis, the total energy is 0.042 and 0.072 meV/Cr higher, respectively, and the value along the z axis is in agreement with another theoretical result of 0.078 meV/Cr [70]. It is noted that the calculated total energy for the state with magnetization along the in-plane direction is 0.025 meV/Cr lower in $Cr_2Ge_2Te_6$ monolayer [7] and 0.263 meV/Cr higher in CrI_3 monolayer [8] when compared with the magnetic state of out-of-plane magnetization. On the other hand, the antiferromagnetic coupling between the in-plane two Cr^{3+} ions is 58.86 meV/Cr higher than the ferromagnetic ground state. This result agrees with previous ground-state calculations [70]. For multilayer systems, the local magnetic moment still prefers the y axis, with the magnetic moment antiparallel with each other between neighboring layers [12].

As indicated by the band structure in Fig. 3, this monolayer of CrSBr is a direct-band-gap semiconductor with the top of the valence band and the bottom of the conduction band both located at the Γ point. The band gap increases a little along the x direction and increases sharply along the orthogonal direction, i.e., $\Gamma \rightarrow Y$. Clearly, this monolayer structure shows anisotropic band dispersion. On the other hand, the two spin channels are well separated in the ferromagnetic ground state.

It should be pointed out that what we have simulated is a suspended monolayer, i.e., a single layer of CrSBr in vacuum. The strength of the Coulomb interaction in such material originates from weak dielectric screening in the 2D limit. For distances exceeding a few nanometers, the screening is determined by the immediate surroundings of the material, which can be vacuum or air in the ideal case of suspended samples. Compared to MoS_2 [44] and blue phosphorene [57], such unique 2D dielectric screening in CrSBr should also be anisotropic. The static screened Coulomb interaction is constructed as [44]

$$W_{\mathbf{GG'}}(\boldsymbol{q}; 0) = \varepsilon_{\mathbf{GG'}}^{-1}(\boldsymbol{q}; 0) v(\boldsymbol{q} + \mathbf{G'}). \tag{3}$$

The effective static 2D dielectric function $\varepsilon_{2D}(q)$ could be obtained [44],

$$\varepsilon_{2D}^{-1}(\boldsymbol{q}) = \frac{|\boldsymbol{q}|}{2\pi e^2 L_z} \sum_{\mathbf{G}_z \mathbf{G}'_z} W_{\mathbf{G}_z \mathbf{G}'_z}(\boldsymbol{q}), \tag{4}$$

where the complicated details of the screening in the out-of-plane direction z have been integrated out. The dielectric screening in such a system obeys particular wavelength

FIG. 5. The lowest valence to conduction-band transition energy (based on quasiparticle energies).
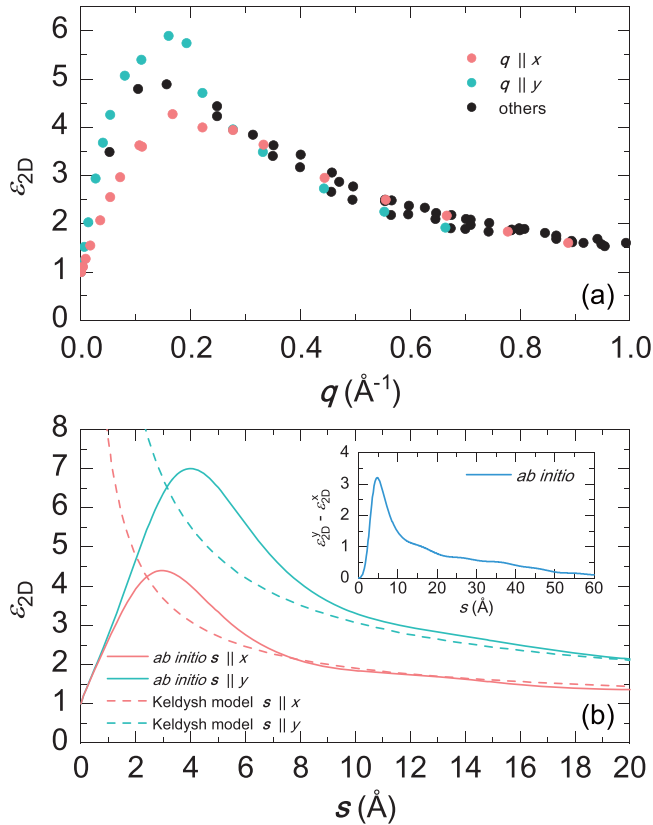
FIG. 4. (a) Frequency dependence of 2D dielectric screening in CrSBr monolayer under *ab initio* calculation. (b) Distance dependence of 2D dielectric screening in CrSBr monolayer under *ab initio* calculation (solid line) and Keldysh model (dashed line). Inset of (b) shows the difference between $\varepsilon_{2D}(s)$ along the y and x axis.

dependence. As demonstrated in Fig. 4(a), in the long-distance limit the electron-electron interacts like that in vacuum with $\varepsilon = 1$, while within the intermediate distance, the electron-electron interaction has effective dielectric screening by the 2D materials with $\varepsilon \geqslant 1$. The label "others" in Fig. 4(a) refers to the other $\boldsymbol{q}$ points in the q mesh which do not belong to $(q_x, 0)$ or $(0, q_y)$. For the anisotropic nature, the dielectric screening changes along different directions. To accurately access the distance dependence of 2D dielectric screening, we have obtained $\varepsilon_{2D}(s)$ through Hankel transformation of $\varepsilon_{2D}(q)$ and shown it in Fig. 4(b). Clearly, if two charges are very close together, there is not enough space for the electronic cloud to polarize, so $\varepsilon_{2D}(s \to 0) = 1$. On the other hand, if the two charges are very far away, the field lines connecting the charges travel mainly through the vacuum, so they are not much affected by the intrinsic dielectric environment of the quasi-2D semiconductor and $\varepsilon_{2D}(s \to \infty) = 1$. Between these two ends, $\varepsilon_{2D}(s)$ is influenced by the intrinsic material property of CrSBr monolayer and is larger than 1. At finite distance $s_{\max}$, $\varepsilon_{2D}(s_{\max})$ will exhibit its maximum. Such 2D dielectric screening has also been revealed in MoS$_2$ monolayer with $s_{\max} = 1.5$ Å and $\varepsilon_{2D}(s_{\max}) = 11$ [44]. For the CrSBr monolayer, $s_{\max}$ is a little larger and $\varepsilon_{2D}(s_{\max})$ is weaker. In the meantime, due to its anisotropic crystal structure, the 2D dielectric screening in CrSBr monolayer also exhibits strong anisotropy. $\varepsilon_{2D}(s_{\max})$ is 4.4 and 7.0 for $\varepsilon_{2D}(s)$ along the x
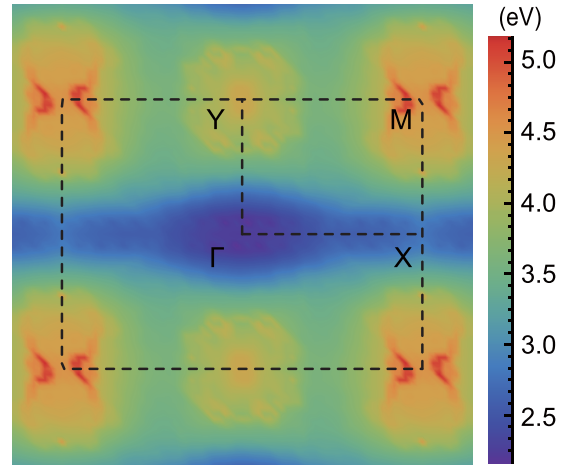
and y axis, respectively, and the corresponding $s_{\max}$ is 3.0 and 4.0 Å, the same order with lattice constants. Interestingly, such anisotropy persists to long distance. As shown in the inset of Fig. 4(b), the difference between $\varepsilon_{2D}(s)$ along the x and y axis does not vanish until 60 Å. So at the distance from 1 Å to ten times length of lattice constant, the anisotropic dielectric screening dominates Coulomb interaction in the CrSBr monolayer. For 2D systems, Coulomb potential could be described by the Keldysh model [17], where the potential between two charges has the form

$$V_{2D}(s) = \frac{\pi e^2}{2\rho_0}\left[H_0\left(\frac{|s|}{\rho_0}\right) - Y_0\left(\frac{|s|}{\rho_0}\right)\right]. \qquad (5)$$

Here H_0 and Y_0 are, respectively, the Struve and Bessel functions of the second kind. ρ_0 is a screening length, which is $\rho_0 = 2\pi\alpha_{2D}$, and α_{2D} is the 2D polarizability. Taking the 2D Fourier transform of Eq. (5) results in a dielectric function of the form

$$\varepsilon_{2D}(\boldsymbol{q}) = 1 + \rho_0|\boldsymbol{q}|. \qquad (6)$$

We fit the Keldysh model to our *ab initio* effective dielectric function at small $\boldsymbol{q}$, where the Coulomb potential approaches $1/s$. The 2D polarizability, however, shows a large difference between the orthogonal two directions. α_{2D} is 4.2 Å for $\boldsymbol{q}$ along the x axis and 10.4 Å for $\boldsymbol{q}$ along the y axis. Based on the above discussion, in sufficiently long range from 1 Å to 60 Å, the dielectric screening in CrSBr monolayer is anisotropic.

Due to the unique dielectric environment (monolayer 2D material suspended in vacuum or other dielectric surroundings), electron-electron and electron-hole interactions in 2D materials are much stronger than conventional bulk materials, like GaAs, Si, and so on. Therefore dielectric screening in 2D materials is reduced compared with conventional bulk materials. With the reduced dielectric screening in 2D CrSBr monolayer, the quasiparticle correction to the electronic band structure is large. At the Γ point, the quasiparticle band gap is 2.22 eV, where the value is 0.50 eV within PBE. In Fig. 5 we have shown the direct quasiparticle band gap in the Brillouin zone. The one-dimensional nature of the lowest transition energies is obvious.
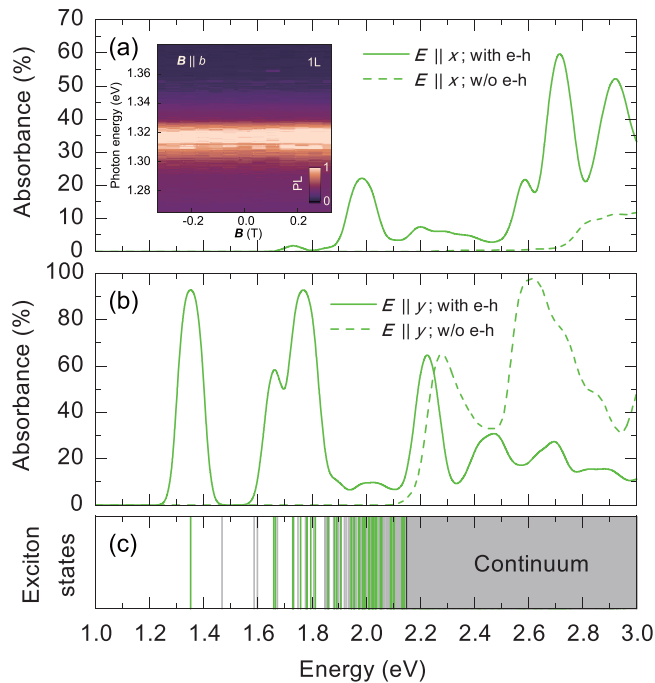
FIG. 6. Anisotropic optical absorbance with electric polarization along the x axis (a) and y axis (b) and corresponding exciton spectrum (c) in CrSBr monolayer. Here, green lines are for the bright excitons and the gray lines are for dark excitons. The dotted lines are for the optical absorption based on IPA. Inset shows the experiment data of PL spectrum of CrSBr monolayer under magnetic field along y axis [12].
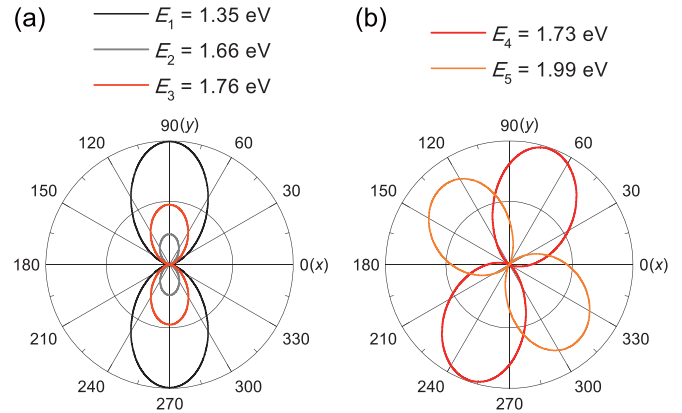

FIG. 7. Optical anisotropy (absorbance amplitude) for the five excitonic states with wavelengths of 1.35 eV (918 nm), 1.66 eV (747 nm), 1.76 eV (705 nm), 1.73 eV (716 nm), and 1.99 eV (623 nm), respectively.

The optical absorbance in CrSBr monolayer is further calculated and shown in Fig. 6, where the difference between two in-plane orthogonal directions is obvious. Although the main optical absorption is located at 3.01 eV, the small peak located below could catch as high as 20% of the incident light. The optical absorption edge is located at 1.35 eV when the electric field is along the y direction. For the other direction, the absorption edge is 1.73 eV. Compared with the results without the consideration of electron-hole interaction, the excitonic effect is obvious in this 2D material. In Fig. 6(c) the exciton states are demonstrated and agree with the optical spectrum well. Dark excitons are also indicated in these non-Rydberg series. Clearly the binding energy for the first exciton state could reach as high as 1.0 eV, almost 1/3 of the quasiparticle band gap for the center of electron-hole excitations. When the electric field is rotated along the xy plane, as shown in Fig. 7 for several bright exciton states, the oscillator strength shows an anisotropic distribution.

We now look at the character of the first eight excitons, which are all excited around the Γ point. In Fig. 8 we show the modulus squared of the real-space exciton wave function when the hole is fixed near a Cr atom. Electron-hole pair amplitudes (the envelope functions) of low-energy exciton wave functions in reciprocal space are plotted in the down panel of each figure. From these plots the nodal structures of the envelope functions of the states are apparent. The 1s state has only one node with the strongest transition at Γ point. In detail, in Fig. 8(a) the character of the exciton corresponding

to the first peak in the absorption spectrum (E ∥ y) reflects the transitions from the top of the valence band to the lowest conduction band around the Γ point. The envelope of the exciton wave function is almost azimuthally symmetric. The root-mean-square radius of the exciton in real space is around 1.4 nm. The second excitonic state is a dark exciton. It is also a 1s state and also arises from the electron-hole excitations around the Γ point, but the orbitals for the electron-hole formation are different from the first bright state. Although it has a much smaller oscillator strength, the electric polarization along the y direction is much higher than that along the x direction. The next two dark excitons shown in Figs. 8(c) and 8(d) are 2p states. The bright exciton shown in Fig. 8(e) is a 2s state, and the exciton in Fig. 8(h) is a 3d state. Together with the first state, these five states could be categorized into the series of electron-hole excitations from v1 to c1 mainly at the Γ point. This can also be judged from the energy distribution in Fig. 9, where the distribution of the constituent free electron-hole pairs specified by (E_v, E_c) for selected exciton states weighted by the module squared exciton envelope function for each specific interband transition is plotted for all these eight excitonic states. Clearly, these five states have similar patterns. As shown in Appendix C, the orbitals corresponding to the electron-hole pairs are Cr d_{yz} and Cr $d_{x^2-y^2}$ [71]. For the second and sixth excitons, it involves v1 to c2 transitions, i.e., from Cr d_{yz} to Cr $d_{x^2-y^2}$ hybrid with S 3p. These transitions bring the above-mentioned dark 1s state in Fig. 8(b) and the bright 2p state in Fig. 8(f). For the exciton shown in Fig. 8(g), it involves more complicated electron-hole pair formation [from v2 to c1 and v1 to c2, as indicated in Fig. 9(g)], and it is a dark state. Characterization of all the node structures of these excitons is summarized in Table I. Obviously, these excitons process an increased real-space extension of the wave function. The effective electron-hole interaction is therefore reduced strongly, consistent with the smaller binding energy as shown in Table I. The difference in the oscillator strength between the x and y direction is obvious for all the exciton states.

With the above revealed anisotropic quasiparticle electronic band structure, electron-hole excitation, and optical
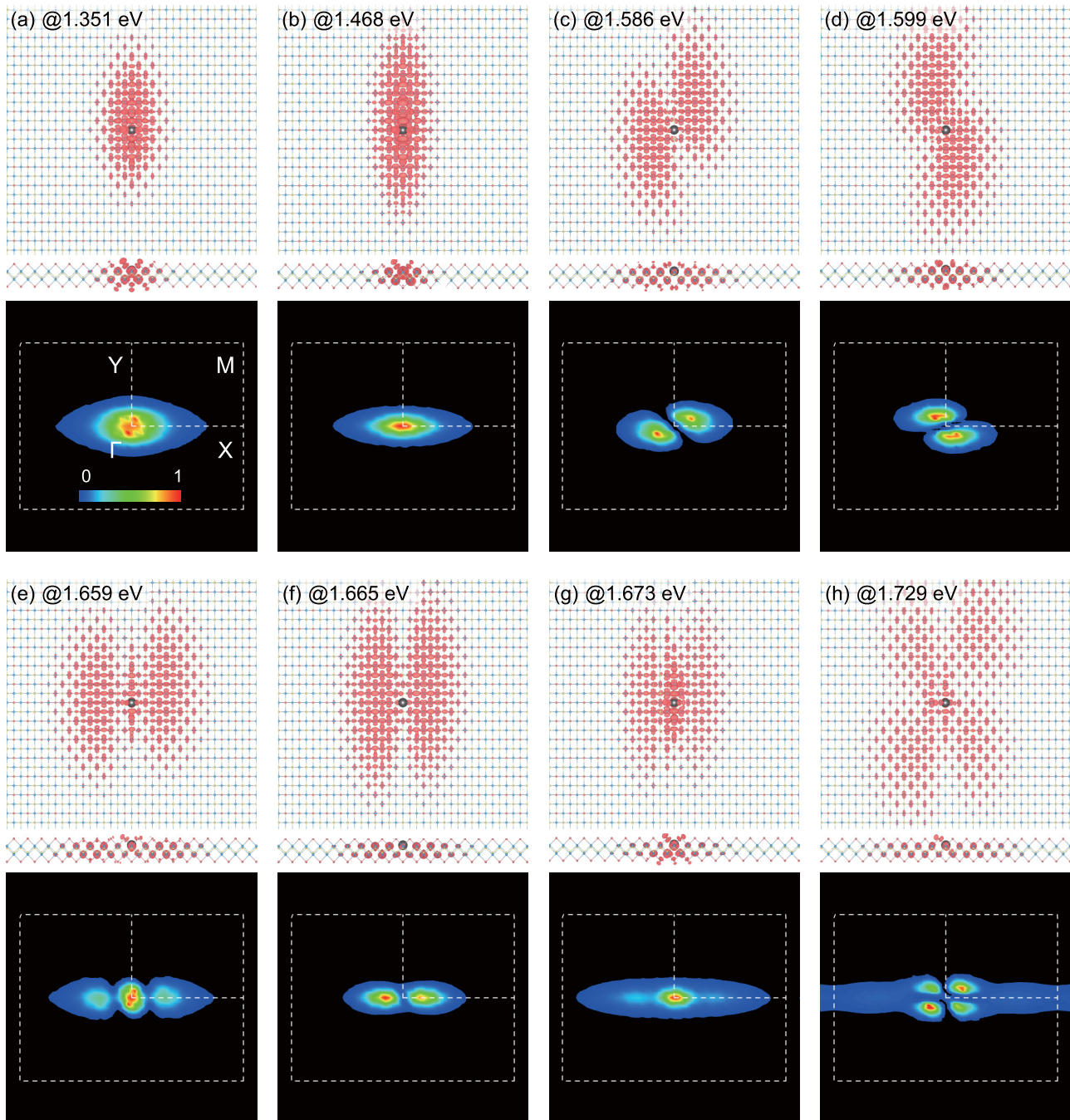
FIG. 8. Real-space plots (upper panel) of modulus squared of the exciton wave function and corresponding reciprocal-space plots (down panel) for the first eight excitons. Here the hole (black circle) is fixed at Cr.

absorption, we continue to show the (magnetic) linear dichroism and MO SH and Voigt effects in CrSBr monolayer. The essence of a theoretical modeling of the MO effects lies in accurately accounting for the diagonal and off-diagonal frequency-dependent macroscopic dielectric functions, which have been readily available from our G_0W_0-BSE calculations with electron-hole interaction included. As verified by the agreement between our theoretical calculations and experiments of CrSBr, as well as the fact that the exciton effect in ferromagnetic monolayer CrI_3 and $CrBr_3$ has strongly modified its MO responses [9,10], significantly different behaviors going beyond those from a treatment considering only

transitions between noninteracting Kohn-Sham orbitals should be expected in CrSBr. To simulate the experimental setup, as demonstrated in Fig. 1, we consider CrSBr monolayer deposited on a dielectric substrate α-Al_2O_3, which has a wide band gap of 8.7 eV with refraction constant of 1.75 [10]. Assuming a linearly polarized incident light, we calculate the SH and Voigt signals by analyzing the polarization plane of the reflection (transmission) light, which is in general elliptically polarized with a rotation angle and an ellipticity. The detailed calculations are based on the transfer matrix method and could be found in Appendix D. In Fig. 10 we have found that the rotation angle could be larger than 10° for the
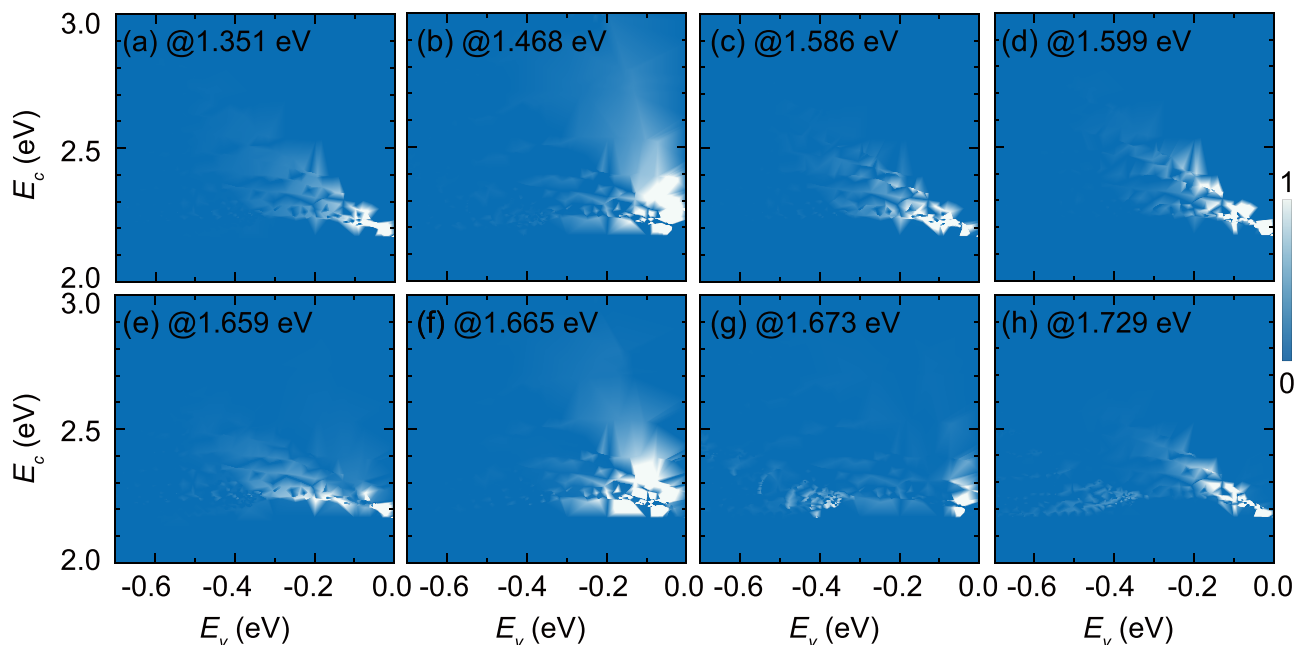
FIG. 9. The distribution of free electron-hole pair with electron energy at E_c and hole energy at E_v for selected exciton states weighted by module squared exciton envelope function for each of the interband transitions between states $|\mathbf{v}\mathbf{k}\rangle$ and $|\mathbf{c}\mathbf{k}\rangle$, with quasiparticle energies of E_{vk}^{QP} and E_{ck}^{QP}, respectively.

reflected light. For transmitted light the largest rotation angle is around $8°$. On the other hand, the revealed SH and Voigt effects dominate within the quasiparticle band gap. When the electron-hole interaction is not considered, both the amplitude and the position of the spectrum are modified significantly (see Fig. 15 in Appendix E). This verifies again the fact that it is the exciton effect that leads to the large linear dichroism in CrSBr monolayer. In addition, we can find that the off-diagonal component of dielectric function plays little role in the above-revealed large linear dichroism in CrSBr, where as shown in Fig. 16 (Appendix E), θ_{SH} and θ_{V} do not change.

We have also performed the calculations of magneto-optical effects when spin orientation is pointing along the x and z axis. As shown in Figs. 17 and 18 (Appendix F), the absorbance spectrum and exciton states are similar to those for the state with spin orientation along the y axis. In the meantime, due to extremely small ε_{yz}, the revealed

rotation angle of the long axis of the polarization ellipse for reflection and transmission light is still determined by the large ratio of $\varepsilon_{xx}/\varepsilon_{yy}$ (see Fig. 19 in Appendix G). On the other hand, when spin orientation is tuned by an external perpendicular magnetic field towards the out-of-plane direction, i.e., the z axis, the magneto-optical Kerr and Faraday effects will appear in the CrSBr monolayer. In this case, a linearly polarized continuous-wave light is modified by the presence of an out-of-plane magnetic field when

TABLE I. Excitonic properties of first eight excitons with excitation energy (E_{xct}), exciton binding energy (E_b), and oscillator strength for electric field along x and y directions.

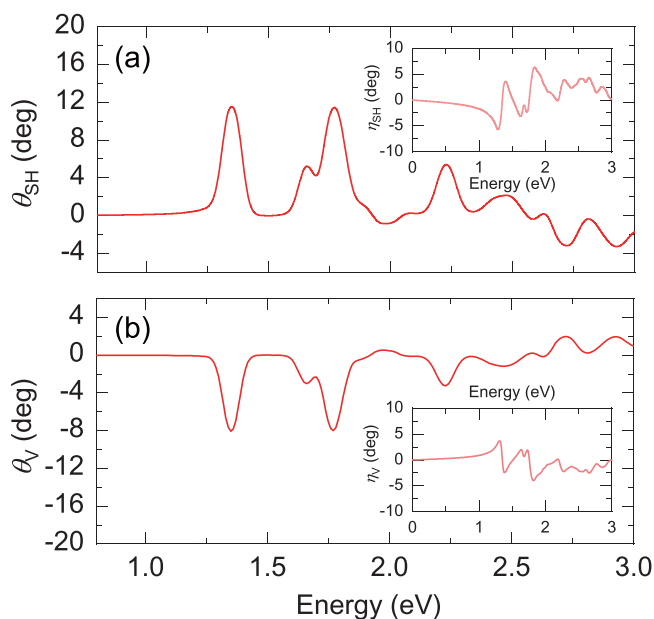| Excitons	E_{xct} (eV)	E_b	Oscillator strength	
			$\boldsymbol{E} \parallel x$	$\boldsymbol{E} \parallel y$
1	1.351	0.870	1.9×10^{-3}	2.3×10^{4}
2	1.468	0.735	2.7×10^{-6}	3.2×10^{-4}
3	1.586	0.635	3.6×10^{-2}	4.7×10^{0}
4	1.599	0.622	2.8×10^{-3}	4.1×10^{0}
5	1.659	0.562	6.4×10^{-1}	5.8×10^{3}
6	1.665	0.556	1.2×10^{-1}	4.6×10^{2}
7	1.673	0.548	3.8×10^{-4}	5.0×10^{-1}
8	1.729	0.492	8.3×10^{1}	3.8×10^{2}

FIG. 10. Rotation angles of (a) reflected and (b) transmitted light in CrSBr monolayer. Insets are ellipticity.

TABLE II. Comparison of magneto-optical effects for reflection and transmission lights, polarization of lights propagating in CrSBr monolayer, off-diagonal elements, and maximums of corresponding rotation angles with electron-hole interaction when spin orientation is along x, y, and z axis in the energy range of $0 \sim 3$ eV.

Spin orientation	Magneto-optical effects	Polarization	Off-diagonal elements	Rotation (°)
x	SH/Voigt	linear	ε_{yz}	11.6/8.1
y	SH/Voigt	linear	ε_{xz}	11.6/8.1
z	Kerr/Faraday	circular	ε_{xy}	1.1/0.6

propagating through CrSBr monolayer. The left- and right-circularly polarized components will propagate with different refractive index and will pick up different optical path length and absorption. Therefore the reflected or transmitted light becomes elliptically polarized (characterized by an ellipticity η), and the long axis of the polarization ellipse is rotated (characterized by a rotation angle θ). The detailed theoretical calculations of rotation angles and ellipticities are shown in Appendix H. Meanwhile, as shown in Fig. 21 (Appendix H), the maximal rotation angles of Kerr and Faraday effects are 1.1° and 0.6°, respectively, which are even larger than 0.9° and 0.3° in CrI$_3$ [9] and 0.3° and 0.2° in CrBr$_3$ [10]. Similar to the cases with in-plane magnetization, the optical spectrum has been modified significantly for the exciton effects (see Fig. 22 in Appendix H). We list the maximal rotation angles in Table II for different spin orientations. Therefore for both linearly and circularly polarized light, the large phase shift facilitates the applications of CrSBr monolayer as optical polarizers and waveplates.

For black phosphorene, it is noted that the ratio between the long axis and short one is 1.4 for the anisotropic crystal structure, and a 1.5-eV energy difference between absorption edges for the electric field along two axes could be found (see Fig. 23 in Appendix I). For comparison, it is noted that the rotational angle in black phosphorene is of similar magnitude. However, CrSBr shows two broad peaks at the energies of both infrared and red lights, whereas black phosphorene exhibits a single narrow peak in this energy window

(see Fig. 24 in Appendix I). Additionally, obvious linear dichroism has been revealed experimentally in black phosphorene and its few layers [72–75]. Therefore, a polarization-sensitive broadband photodetector using a CrSBr vertical p-n junction could be constructed successfully for the application in 2D semiconductor optoelectronics.

To demonstrate other potential applications in 2D semiconductor optoelectronics, we further calculate the lifetime of the first bright exciton. Using "Fermi's golden rule," the radiative lifetime $\tau_S(0)$ at 0 K of an exciton in state S is derived according to [76,77]

$$\tau_S(0) = \frac{\hbar^2 c}{8\pi e^2 E_S(0)} \frac{A_{uc}}{\mu_S^2}, \qquad (7)$$

where c is the speed of light, A_{uc} is the area of the unit cell, $E_S(0)$ is the energy of the exciton in state S, and $\mu_S^2 = (\hbar^2/m^2 E_S(0)^2)(|\langle G|p_{||}|\Psi_S\rangle|^2/N_k)$ is the square modulus of the BSE exciton transition dipole divided by the number of unit cells in this 2D system. The exciton radiative lifetime $\langle \tau_S \rangle$ at temperature T is obtained as

$$\langle \tau_S \rangle = \tau_S(0)\frac{3}{4}\left(\frac{E_S(0)^2}{2M_S c^2}\right)^{-1} k_B T, \qquad (8)$$

where k_B is Boltzmann's constant, and $M_S = m_e^* + m_h^*$ is the exciton effective mass. The computed radiative lifetime of the first bright exciton in CrSBr monolayer at 4 and 300 K is 0.001 and 0.100 ns, respectively, which is even smaller than those in the conventional transition-metal dichalcogenides, e.g., 0.004 and 0.270 ns in MoS$_2$ [77]. In Table III we have listed the exciton lifetime of some typical 2D semiconductors [56,57,59,64,77–86], as well as conventional semiconductor GaInN/GaN quantum wells [87]. Clearly, such a short lifetime in CrSBr monolayer together with its direct band gap shows its advantages in infrared light-emitting applications. Moreover, as shown in Fig. 11, the strong optical absorption of CrSBr monolayer covering the whole solar spectrum as well as its optimized band gap (1.35 eV) within the Shockley-Queisser limit also suggests efficient solar energy conversion. Therefore, from gapless graphene to narrow-band-gap black phosphorene, intermediate-band-gap transition-metal dichalcogenides, and wide-band-gap semi-

TABLE III. Collection of exciton radiative lifetime τ (ns) for various 2D materials. τ_S^{LT} and τ_S^{RT} are the computed radiative lifetimes at low temperature (≈ 4 K) and room temperature, respectively. Experimental data of τ_{exp}^{LT} and τ_{exp}^{RT} are also listed for comparison.

|	τ_S^{LT}	τ_S^{RT}	τ_{exp}^{LT}	τ_{exp}^{RT}
CrSBr monolayer	0.001	0.100		
Black phosphorus monolayer	3×10^{-5} [56]	0.002 [56]		0.221 [78]
Hittorf's phosphorus monolayer	0.24 [59]	18 [59]		
GeS monolayer	7×10^{-5} [56]	0.005 [56]		
ReS$_2$ monolayer				0.04 [79]
Blue phosphorus monolayer	0.003 [57]	0.24 [57]		
MoS$_2$ monolayer	0.004 [77]	0.27 [77]	0.005 [80], 0.005 [81]	0.85 [82]
MoSe$_2$ monolayer	0.005 [77]	0.38 [77]	0.002 [83]	0.9 [84]
WS$_2$ monolayer	0.002 [77]	0.17 [77]		
WSe$_2$ monolayer	0.004 [77]	0.29 [77]	0.002 [83], 0.004 [85]	4 [86]
2D GaN			0.6 [64]	
GaInN/GaN QW				10^2 [87]
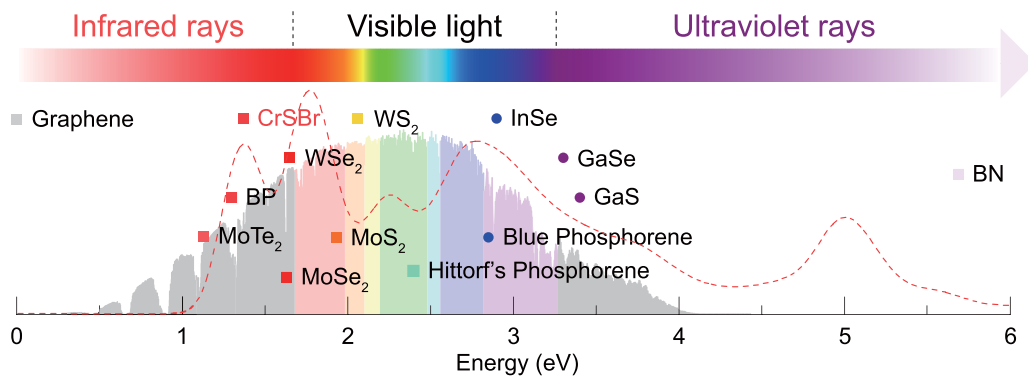
FIG. 11. Some 2D materials covering a broad spectral range, from gapless graphene to narrow-band-gap black phosphorene, intermediate-band-gap transition-metal dichalcogenides, and wide-band-gap semiconductors of Hittorf's phosphorene, blue phosphorene, III-V monochalcogenides, and boron nitride. Squares and circles represent direct- and indirect-band-gap semiconductors, respectively. The solar spectrum [88] and averaged absorbance (dashed red line) of light polarized along the x and y axis in CrSBr monolayer are also shown.

conductors of Hittorf's phosphorene, blue phosphorene, III-V monochalcogenides, and boron nitride, magnetic CrSBr could play an important role in infrared optoelectronics and 2D photovoltaics.

IV. SUMMARY

To summarize, by considering explicitly many-body effects of the electron-electron and electron-hole interactions in 2D ferromagnet CrSBr, we have demonstrated unusual large optical anisotropy in this 2D material. The inherent in-plane magnetization with the consideration of spin-orbit coupling is found to contribute little to the revealed large linear dichroism. The giant SH and Voigt effects, which are comparable with those in black phosphorene, originate from the inherent anisotropic crystal structure and coherent one-dimensional band dispersion for anisotropic electron-hole pair excitation. Our calculation of the first exciton located at 1.35 eV agrees with a recent experiment of photoluminescence. The in-gap exciton states of either bright or dark show the diversity of electron-hole excitation in this 2D magnet. Compared with black phosphorene, the relative delocalization of exciton in k space indicates the nature of electron-hole excitation in CrSBr is in-between Wannier-Mott type and Frenkel type. The excitonic effect has modified ε_{xx}, ε_{yy}, and ε_{xz} dramatically and, consequently, the linear dichroism and the magneto-optical properties. With out-of-plane magnetization, Kerr and Faraday effects have been revealed in CrSBr monolayer that are even larger than those in CrI$_3$ and CrBr$_3$. Furthermore, the short exciton lifetime as well as the strong optical absorption covering the whole solar spectrum shows its advantages in the application of light-emitting diodes and solar cells. Our studies have provided a basic framework to account for the high-order magneto-optical effects in 2D magnets and have also shown potential applications of CrSBr in 2D optics and optoelectronics.

ACKNOWLEDGMENTS

APPENDIX A: BASIC FRAMEWORK OF GW-BSE IN BERKELEYGW PACKAGE

Generally, the quasiparticle self-energies are obtained by solving the Dyson equation [26]:

$$\left[-\tfrac{1}{2}\nabla^2 + V_{\text{ion}} + V_{\text{H}} + \Sigma\big(E_{n\mathbf{k}}^{\text{QP}}\big)\right]\psi_{n\mathbf{k}}^{\text{QP}} = E_{n\mathbf{k}}^{\text{QP}}\psi_{n\mathbf{k}}^{\text{QP}}, \quad \text{(A1)}$$

where Σ is the self-energy operator within the GW approximation, and $E_{n\mathbf{k}}^{\text{QP}}$ and $\psi_{n\mathbf{k}}^{\text{QP}}$ are the quasiparticle energies and wave functions, respectively. The self-energy operator Σ is invoked for the quasiparticle behavior with quasiparticle energies $E_{n\mathbf{k}}^{\text{QP}}$ and wave functions $\psi_{n\mathbf{k}}^{\text{QP}}$. Here we use the many-body perturbation method with one-shot G_0W_0 framework. The mean-field wave functions within DFT-PBE are used as quasiparticle wave functions, and the quasiparticle energy is approached starting from the DFT-PBE eigenvalue.

We first compute static polarizability based on the random-phase approximation (RPA) [26]:

$$\chi_{\mathbf{GG'}}(\mathbf{q};0) = \sum_{n,n',\mathbf{k}} \langle n,\mathbf{k}|e^{-i(\mathbf{q}+\mathbf{G})\cdot\mathbf{r}}|n',\mathbf{k}+\mathbf{q}\rangle\langle n',\mathbf{k}$$

$$+\mathbf{q}|e^{i(\mathbf{q}+\mathbf{G'})\cdot\mathbf{r'}}|n,\mathbf{k}\rangle\frac{1}{E_{n'\mathbf{k}+\mathbf{q}} - E_{n\mathbf{k}}}, \quad \text{(A2)}$$

where n, n' are occupied and unoccupied band indices, $\mathbf{k}$ is a wave vector, $\mathbf{q}$ is a vector in the first Brillouin zone, $\mathbf{G}$ is a reciprocal-lattice vector, and $|n,\mathbf{k}\rangle$ and $E_{n\mathbf{k}}$ are the mean-field electronic eigenvectors and eigenvalues, respectively.

Then the dielectric matrix is constructed as [26]

$$\varepsilon_{\mathbf{GG'}}(\mathbf{q};0) = \delta_{\mathbf{GG'}} - v(\mathbf{q}+\mathbf{G})\chi_{\mathbf{GG'}}(\mathbf{q};0), \quad \text{(A3)}$$

with the slab-truncated Coulomb interaction included [30],

$$v_{\text{t}}^{\text{slab}}(\mathbf{q}) = \frac{4\pi}{q^2}[1 - e^{-q_{xy}\cdot z_c}\cos(q_z z_c)], \quad \text{(A4)}$$

where z_c is the truncation distance in the perpendicular direction. Such kinds of treatment could guarantee the convergence of dielectric screening ("head" in $\varepsilon_{\mathbf{GG'}}$) to approach the unit in the long-wavelength limit.

Within the generalized plasmon pole (GPP) model, the imaginary and real part inverse dielectric matrix with finite frequencies are given by [26]

$$\mathrm{Im}\varepsilon_{\mathbf{GG'}}^{-1}(\mathbf{q}, \omega) = -\frac{\pi}{2} \frac{\Omega_{\mathbf{GG'}}(\mathbf{q})}{\tilde{\omega}_{\mathbf{GG'}}(\mathbf{q})} \{\delta[\omega - \tilde{\omega}_{\mathbf{GG'}}(\mathbf{q})] - \delta[\omega + \tilde{\omega}_{\mathbf{GG'}}(\mathbf{q})]\}, \quad (A5)$$

and

$$\mathrm{Re}\varepsilon_{\mathbf{GG'}}^{-1}(\mathbf{q}, \omega) = 1 + \frac{\Omega_{\mathbf{GG'}}^2(\mathbf{q})}{\omega^2 - \tilde{\omega}_{\mathbf{GG'}}^2(\mathbf{q})}, \quad (A6)$$

where $\Omega_{\mathbf{GG'}}(\mathbf{q})$ and $\tilde{\omega}_{\mathbf{GG'}}(\mathbf{q})$ are the effective bare plasma frequency and the GPP mode frequency, defined as [26]

$$\Omega_{\mathbf{GG'}}^2(\mathbf{q}) = \omega_{\mathrm{p}}^2 \frac{(\mathbf{q} + \mathbf{G}) \cdot (\mathbf{q} + \mathbf{G'})}{|\mathbf{q} + \mathbf{G}|^2} \frac{\rho(\mathbf{G} - \mathbf{G'})}{\rho(\mathbf{0})}, \quad (A7)$$

$$\tilde{\omega}_{\mathbf{GG'}}^2(\mathbf{q}) = \frac{\Omega_{\mathbf{GG'}}^2(\mathbf{q})}{\delta_{\mathbf{GG'}} - \varepsilon_{\mathbf{GG'}}^{-1}(\mathbf{q}, \omega = 0)}. \quad (A8)$$

Here ρ is the electron charge density in reciprocal space, and $\omega_{\mathrm{p}}^2 = 4\pi \rho(\mathbf{0})e^2/m$ is the classical plasma frequency.

Using the form of the above frequency-dependent dielectric function, the self-energy operator Σ is solved in two parts, $\Sigma = \Sigma_{\mathrm{SEX}} + \Sigma_{\mathrm{COH}}$, where Σ_{SEX} is the screened exchange operator and Σ_{COH} is the Coulomb-hole operator [26],

$$\langle n, \mathbf{k}|\Sigma_{\mathrm{SEX}}(E)|n', \mathbf{k}\rangle = -\sum_{n_1}^{\mathrm{occ}} \sum_{\mathbf{q},\mathbf{G},\mathbf{G'}} \langle n, \mathbf{k}|e^{i(\mathbf{q}+\mathbf{G})\cdot\mathbf{r}}|n_1, \mathbf{k} - \mathbf{q}\rangle \langle n_1, \mathbf{k} - \mathbf{q}|e^{-i(\mathbf{q}+\mathbf{G'})\cdot\mathbf{r'}}|n', \mathbf{k}\rangle$$

$$\times \left(1 + \frac{\Omega_{\mathbf{GG'}}^2(\mathbf{q})}{\left(E - E_{n_1\mathbf{k}-\mathbf{q}}\right)^2 - \tilde{\omega}_{\mathbf{GG'}}^2(\mathbf{q})}\right) v(\mathbf{q} + \mathbf{G'}), \quad (A9)$$

and

$$\langle n, \mathbf{k}|\Sigma_{\mathrm{COH}}(E)|n', \mathbf{k}\rangle = \sum_{n_1} \sum_{\mathbf{q},\mathbf{G},\mathbf{G'}} \langle n, \mathbf{k}|e^{i(\mathbf{q}+\mathbf{G})\cdot\mathbf{r}}|n_1, \mathbf{k} - \mathbf{q}\rangle \langle n_1, \mathbf{k} - \mathbf{q}|e^{-i(\mathbf{q}+\mathbf{G'})\cdot\mathbf{r'}}|n', \mathbf{k}\rangle$$

$$\times \frac{1}{2} \frac{\Omega_{\mathbf{GG'}}^2(\mathbf{q})}{\tilde{\omega}_{\mathbf{GG'}}(\mathbf{q})\left[E - E_{n_1\mathbf{k}-\mathbf{q}} - \tilde{\omega}_{\mathbf{GG'}}(\mathbf{q})\right]} v(\mathbf{q} + \mathbf{G'}). \quad (A10)$$

With the above-obtained quasiparticle energies and static dielectric screening from RPA, the electron-hole excitations are then calculated by solving the BSE for each exciton state S [27]:

$$\left(E_{c\mathbf{k}}^{\mathrm{QP}} - E_{v\mathbf{k}}^{\mathrm{QP}}\right)A_{vc\mathbf{k}}^S + \sum_{v'c'\mathbf{k'}} \langle vc\mathbf{k}|K^{\mathrm{eh}}|v'c'\mathbf{k'}\rangle A_{v'c'\mathbf{k'}}^S = \Omega^S A_{vc\mathbf{k}}^S, \quad (A11)$$

where $A_{vc\mathbf{k}}^S$ is the exciton wave function, Ω^S is the excitation energy, and K^{eh} is the electron-hole interaction kernel.

The kernel contains two terms, a screened direct interaction and a bare exchange interaction, $K^{\mathrm{eh}} = K^{\mathrm{d}} + K^{\mathrm{x}}$, defined as [27]

$$\langle vc\mathbf{k}|K^{\mathrm{d}}|v'c'\mathbf{k'}\rangle = \sum_{\mathbf{GG'}} \langle c, \mathbf{k} + \mathbf{q}|e^{-i(\mathbf{q}+\mathbf{G})\cdot\mathbf{r}}|c', \mathbf{k}\rangle W_{\mathbf{GG'}}(\mathbf{q}; 0)\langle v', \mathbf{k}|e^{i(\mathbf{q}+\mathbf{G'})\cdot\mathbf{r}}|v, \mathbf{k} + \mathbf{q}\rangle \quad (A12)$$

and

$$\langle vc\mathbf{k}|K^{\mathrm{x}}|v'c'\mathbf{k'}\rangle = \sum_{\mathbf{GG'}} \langle c, \mathbf{k} + \mathbf{q}|e^{-i(\mathbf{q}+\mathbf{G})\cdot\mathbf{r}}|v, \mathbf{k}\rangle \delta_{\mathbf{GG'}} v(\mathbf{q} + \mathbf{G})\langle v', \mathbf{k}|e^{i(\mathbf{q}+\mathbf{G'})\cdot\mathbf{r}}|c', \mathbf{k} + \mathbf{q}\rangle. \quad (A13)$$

Finally, we obtain the imaginary parts of frequency-dependent complex dielectric function $\varepsilon_2(\omega)$ as [27]

$$\varepsilon_2(\omega) = \frac{16\pi^2 e^2}{\omega^2} \sum_S |\mathbf{e} \cdot \langle 0|\mathbf{v}|S\rangle|^2 \delta(\omega - \Omega^S), \quad (A14)$$

where $\mathbf{v}$ is the velocity operator and $\mathbf{e}$ is the polarization of the incoming light. Here we use the absorbance $\mathcal{A}$ of 2D materials to measure their optical properties, which is expressed as [62]

$$\mathcal{A}(\omega) = 1 - e^{-\alpha(\omega)d} = 1 - e^{-\frac{\omega\varepsilon_2 d}{\hbar c}}, \quad (A15)$$

where α is the absorption coefficient, d is the thickness of the simulation cell along the direction perpendicular to the layer,

ε_2 is the imaginary part of the dielectric function, and ω is the photon energy.

APPENDIX B: CONVERGENCE OF G_0W_0-BSE CALCULATIONS OF CrSBr MONOLAYER

In Fig. 12 we show the convergence of quasiparticle energies in CrSBr with respect to (a) the scale of k grid (coarse grid), (b) the number of bands, and (c) the dielectric cutoff. It is noted that fine sampling is necessary to capture the rapid variation in screening at small wave vectors and the fine features in the exciton wave functions, which are tightly localized in k space. In Fig. 13, besides the RPA dielectric function, we show the convergence of exciton energy in CrSBr with respect to the scale of the k grid (fine grid).
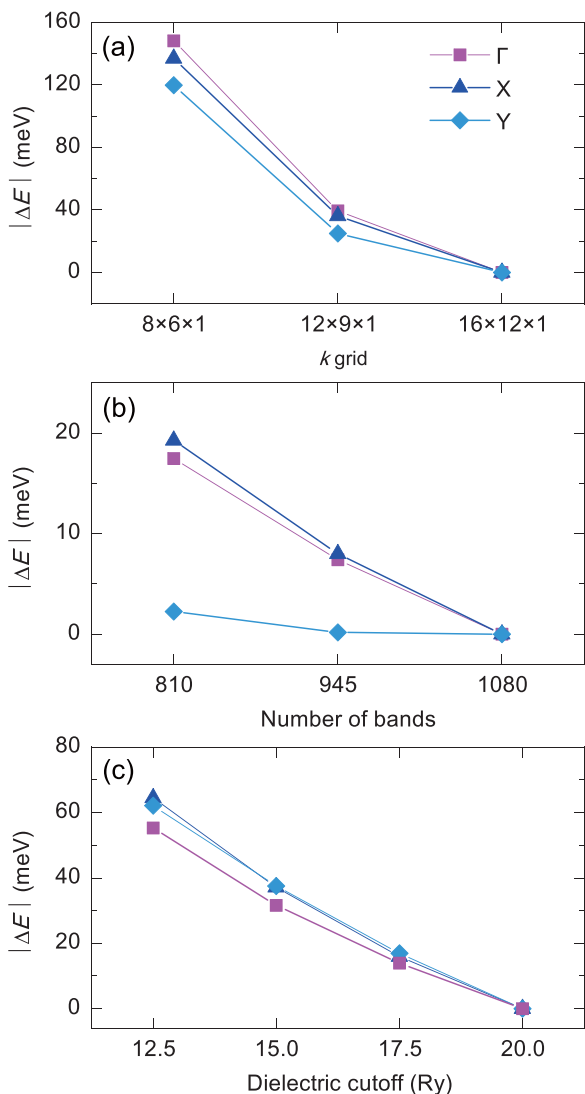
FIG. 12. Convergence of the quasiparticle (G_0W_0) band gap at three high-symmetry k points with respect to the scale of coarse k grid (a), number of bands (b), and dielectric cutoff energy ($\varepsilon_{\text{cutoff}}$) (c). In (a) we use a $\varepsilon_{\text{cutoff}}$ of 20 Ry and 1080 bands; in (b) we use a k grid of $16 \times 12 \times 1$ and 1080 bands; and in (c) we use a $\varepsilon_{\text{cutoff}}$ of 20 Ry and a k grid of $16 \times 12 \times 1$. With the above consideration, we use a $16 \times 12 \times 1$ k grid, a $\varepsilon_{\text{cutoff}}$ of 20 Ry, and 1080 (20 times larger) bands for our G_0W_0 calculations.

APPENDIX C: MAXIMUM LOCALIZED WANNIER ORBITALS IN CRSBR

Using WANNIER90 [71], the orbital-decomposed band structure (PBE level) is shown in Fig. 14.

APPENDIX D: CALCULATIONS OF LINEAR DICHROISM (OPTICAL BIREFRINGENCE) AND SCHÄFER-HUBERT AND VOIGT EFFECTS

As shown in Fig. 1, considering the in-plane magnetization along the y axis ($\boldsymbol{B} = B\hat{e}_y$), the dielectric tensor is expressed
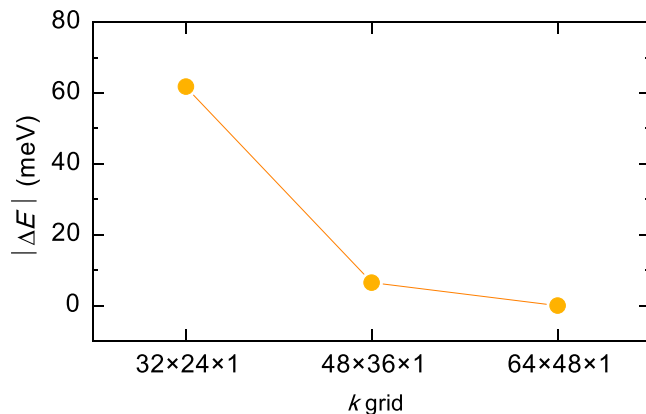

FIG. 13. Convergence of the energy of the $1s$ exciton state in BSE calculations with respect to the scale of the fine k grids, including $32 \times 24 \times 1$, $60 \times 60 \times 1$, $48 \times 36 \times 1$, and $64 \times 48 \times 1$. With the above consideration, we use a $64 \times 48 \times 1$ k grid in our BSE calculations.

as

$$\boldsymbol{\varepsilon}(\omega, \boldsymbol{B}) = \begin{pmatrix} \varepsilon_{xx}(\omega, \boldsymbol{B}) & 0 & \varepsilon_{xz}(\omega, \boldsymbol{B}) \\ 0 & \varepsilon_{yy}(\omega, \boldsymbol{B}) & 0 \\ -\varepsilon_{xz}(\omega, \boldsymbol{B}) & 0 & \varepsilon_{zz}(\omega, \boldsymbol{B}) \end{pmatrix}. \quad \text{(D1)}$$
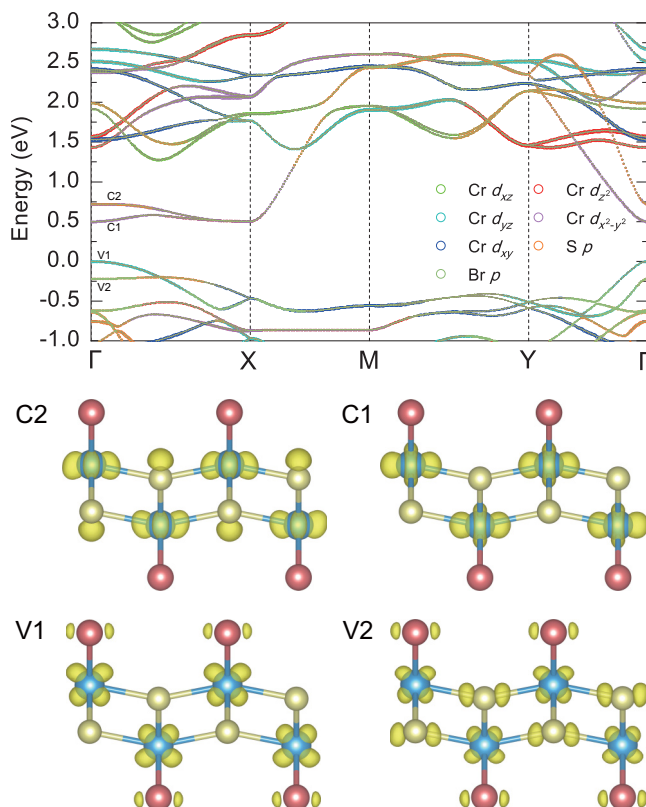

FIG. 14. The up panel shows the orbital-decomposed band structure (DFT-PBE level) of CrSBr from maximum localized Wannier orbitals using WANNIER90 [71]. The partial charge at Γ point is shown in the down panel.

The Fresnel equation for the propagation of the electromagnetic wave is given by

$$[n^2 I - \varepsilon - n : n] \cdot E = 0. \tag{D2}$$

For normal incidence, the complex refractory index **n** is

$$n = \frac{ck}{\omega} = \frac{ck}{\omega} \hat{e}_z. \tag{D3}$$

By solving the above Fresnel equations, we get the normal modes as $\parallel$ and $\perp$ for linearly polarized plane waves which are parallel and perpendicular to $\hat{e}_y$ (magnetization direction), with distinct refractive indices:

$$n_\parallel^2(\omega, B\hat{e}_y) = \varepsilon_{yy}(\omega, B\hat{e}_y), \tag{D4}$$

and

$$n_\perp^2(\omega, B\hat{e}_y) = \varepsilon_{xx}(\omega, B\hat{e}_y) + \frac{\varepsilon_{xz}^2(\omega, B\hat{e}_y)}{\varepsilon_{zz}(\omega, B\hat{e}_y)}. \tag{D5}$$

To mathematically describe how an electromagnetic wave interacts with such stratified and anisotropic media, we adopt a 4×4 formalism involving the in-plane components of both electric (E_x, E_y) and magnetic fields (B_x, B_y). We consider a monolayer material magnetized along the $+y$ direction, and the second layer is vacuum. Within each layer ($l = 0, 1, 2$), we choose the four eigenmodes of light as follows: $\hat{e}_1^{(l)} = \hat{e}_2^{(l)} = \hat{e}_x$, $\hat{e}_3^{(l)} = \hat{e}_4^{(l)} = \hat{e}_y$, with the corresponding refractive indices: $n_1^{(l)} = -n_2^{(l)} = n_\perp^{(l)}$, $n_3^{(l)} = -n_4^{(l)} = n_\parallel^{(l)}$. The electric and magnetic fields of light in the first and second layers are given by

$$E^{(l)} = \sum_{j=1}^{4} E_{0j}^{(l)} \hat{e}_j^{(l)} \exp\left\{i\left[k_j^{(l)}(z - z_{l-1}) - \omega t\right]\right\}, \tag{D6}$$

and

$$cB^{(l)} = \sum_{j=1}^{4} E_{0j}^{(l)} b_j^{(l)} \exp\left\{i\left[k_j^{(l)}(z - z_{l-1}) - \omega t\right]\right\}, \tag{D7}$$

with $b_j^{(l)} = n_j^{(l)} \hat{e}_z \times \hat{e}_j^{(l)}$. The electric and magnetic fields of light in the zeroth layer are given by

$$E^{(0)} = \sum_{j=1}^{4} E_{0j}^{(0)} \hat{e}_j^{(0)} \exp\left\{i\left[k_j^{(0)}(z - z_0) - \omega t\right]\right\} \tag{D8}$$

and

$$cB^{(0)} = \sum_{j=1}^{4} E_{0j}^{(0)} b_j^{(0)} \exp\left\{i\left[k_j^{(0)}(z - z_0) - \omega t\right]\right\}. \tag{D9}$$

The requirement of the continuity of the tangential field components at the interfaces connects the field amplitudes $E_{0j}^{(l)}$ between two neighboring layers. The dynamical matrix within each layer is given by a block-diagonal form:

$$D^{(l)} = \begin{pmatrix} \hat{e}_1^{(l)} \cdot \hat{e}_x & \hat{e}_2^{(l)} \cdot \hat{e}_x & \hat{e}_3^{(l)} \cdot \hat{e}_x & \hat{e}_4^{(l)} \cdot \hat{e}_x \\ \hat{b}_1^{(l)} \cdot \hat{e}_y & \hat{b}_2^{(l)} \cdot \hat{e}_y & \hat{b}_3^{(l)} \cdot \hat{e}_y & \hat{b}_4^{(l)} \cdot \hat{e}_y \\ \hat{e}_1^{(l)} \cdot \hat{e}_y & \hat{e}_2^{(l)} \cdot \hat{e}_y & \hat{e}_3^{(l)} \cdot \hat{e}_y & \hat{e}_4^{(l)} \cdot \hat{e}_y \\ \hat{b}_1^{(l)} \cdot \hat{e}_x & \hat{b}_2^{(l)} \cdot \hat{e}_x & \hat{b}_3^{(l)} \cdot \hat{e}_x & \hat{b}_4^{(l)} \cdot \hat{e}_x \end{pmatrix}$$

$$= \begin{pmatrix} 1 & 1 & 0 & 0 \\ n_\perp^{(l)} & -n_\perp^{(l)} & 0 & 0 \\ 0 & 0 & 1 & 1 \\ 0 & 0 & -n_\parallel^{(l)} & n_\parallel^{(l)} \end{pmatrix}. \tag{D10}$$

The propagation matrix is defined as a diagonal matrix:

$$P^{(1)} = \begin{pmatrix} e^{i\delta_\perp} & 0 & 0 & 0 \\ 0 & e^{-i\delta_\perp} & 0 & 0 \\ 0 & 0 & e^{i\delta_\parallel} & 0 \\ 0 & 0 & 0 & e^{-i\delta_\parallel} \end{pmatrix}, \tag{D11}$$

where $\delta_\perp = \frac{\omega}{c} n_\perp$, $\delta_\parallel = \frac{\omega}{c} n_\parallel$, and d is the thickness of layer 1, i.e., monolayer CrSBr.

In this two-interface setup, $E_0^{(0)}$ and $E_0^{(2)}$ are related by the transfer matrix M_c in the basis of linearly polarized lights:

$$E_0^{(2)} = M_c E_0^{(0)} = [D^{(2)}]^{-1} D^{(1)} P^{(1)} [D^{(1)}]^{-1} D^{(0)} E_0^{(0)}. \tag{D12}$$

M_c has a simple block-diagonal form:

$$M_c = \begin{pmatrix} M_\perp & 0 \\ 0 & M_\parallel \end{pmatrix}, \tag{D13}$$

$$M_\perp = \frac{1}{t_{21}^\perp t_{10}^\perp} \begin{pmatrix} e^{i\delta_\perp} + e^{-i\delta_\perp} r_{21}^\perp r_{10}^\perp & e^{i\delta_\perp} r_{10}^\perp + e^{-i\delta_\perp} r_{21}^\perp \\ e^{i\delta_\perp} r_{21}^\perp + e^{-i\delta_\perp} r_{10}^\perp & e^{i\delta_\perp} r_{21}^\perp r_{10}^\perp + e^{-i\delta_\perp} \end{pmatrix}, \tag{D14}$$

where r_{mn} and t_{mn} are the Fresnel coefficients of the interface from the mth layer to the nth layer, and $M_\parallel$ has the same form. In the left and right layers we adopt a basis transformation from the linearly polarized light ($\hat{e}_x, \hat{e}_y$) to the light ($\hat{e}_a, \hat{e}_b$) with $\hat{e}_a = \frac{1}{\sqrt{2}}(\hat{e}_x + \hat{e}_y)$ and $\hat{e}_b = \frac{1}{\sqrt{2}}(-\hat{e}_x + \hat{e}_y)$. $\hat{e}_1^{(l)} = \hat{e}_2^{(l)} = \hat{e}_a, \hat{e}_3^{(l)} = \hat{e}_4^{(l)} = \hat{e}_b$, and $n_1^{(l)} = -n_2^{(l)} = n_3^{(l)} = -n_4^{(l)} = n^{(l)}$, for $l = 0, 2$. This new basis of linearly polarized plane waves is denoted as $\{a \rightarrow, a \leftarrow, b \rightarrow, b \leftarrow\}$. In this basis of linearly polarized lights, the electric field amplitudes in the left and right layer are related by the transfer matrix M:

$$\begin{pmatrix} E_{0a\rightarrow}^{(2)} \\ E_{0a\leftarrow}^{(2)} \\ E_{0b\rightarrow}^{(2)} \\ E_{0b\leftarrow}^{(2)} \end{pmatrix} = M \begin{pmatrix} E_{0a\rightarrow}^{(0)} \\ E_{0a\leftarrow}^{(0)} \\ E_{0b\rightarrow}^{(0)} \\ E_{0b\leftarrow}^{(0)} \end{pmatrix} \tag{D15}$$

$$M = \frac{1}{2} \begin{pmatrix} M_\perp + M_\parallel & -M_\perp + M_\parallel \\ -M_\perp + M_\parallel & M_\perp + M_\parallel \end{pmatrix}. \tag{D16}$$

Because the angle of electric field of incident light and the direction of magnetization ($+y$) is $45°$, $E_{0b\leftarrow}^{(2)} = 0$. In addition, there are no reflecting lights from the *zero*th medium (semi-infinite substrate) to CrSBr, which means $E_{0a\rightarrow}^{(0)} = E_{0b\rightarrow}^{(0)} = 0$. With these two conditions, by calculating Eq. (D15), we can get

$$t_{ss} \equiv \frac{E_{0a\leftarrow}^{(0)}}{E_{0a\leftarrow}^{(2)}} = \frac{M_{44}}{M_{22} M_{44} - M_{24} M_{42}}, \tag{D17}$$

$$t_{sp} \equiv \frac{E_{0b\leftarrow}^{(0)}}{E_{0a\leftarrow}^{(2)}} = \frac{-M_{42}}{M_{22} M_{44} - M_{24} M_{42}}, \tag{D18}$$

$$r_{ss} \equiv \frac{E_{0a\rightarrow}^{(0)}}{E_{0a\leftarrow}^{(2)}} = \frac{M_{12}M_{44} - M_{14}M_{42}}{M_{22}M_{44} - M_{24}M_{42}}, \quad \text{(D19)}$$

$$r_{sp} \equiv \frac{E_{0b\rightarrow}^{(0)}}{E_{0a\leftarrow}^{(2)}} = \frac{M_{32}M_{44} - M_{34}M_{42}}{M_{22}M_{44} - M_{24}M_{42}}. \quad \text{(D20)}$$

The SH signals for the reflected (right-moving) electric field $E_{\rightarrow}^{(2)} = E_{0a\rightarrow}^{(2)}\hat{e}_a + E_{0b\rightarrow}^{(2)}\hat{e}_b$ are expressed as

$$\tan 2\theta_{\mathrm{SH}} = \frac{2\left|\frac{r_{sp}}{r_{ss}}\right|\cos\left(\arg\frac{r_{sp}}{r_{ss}}\right)}{1 - \left|\frac{r_{sp}}{r_{ss}}\right|^2}, \quad \text{(D21)}$$

$$\sin 2\eta_{\mathrm{SH}} = \frac{2\left|\frac{r_{sp}}{r_{ss}}\right|\sin\left(\arg\frac{r_{sp}}{r_{ss}}\right)}{1 + \left|\frac{r_{sp}}{r_{ss}}\right|^2}. \quad \text{(D22)}$$

Similarly, the Voigt signals for the transmitted (left-moving) electric field $E_{\leftarrow}^{(0)} = E_{0a\leftarrow}^{(0)}\hat{e}_a + E_{0b\leftarrow}^{(0)}\hat{e}_b$ are expressed as

$$\tan 2\theta_{\mathrm{V}} = \frac{2\left|\frac{t_{sp}}{t_{ss}}\right|\cos\left(\arg\frac{t_{sp}}{t_{ss}}\right)}{1 - \left|\frac{t_{sp}}{t_{ss}}\right|^2}, \quad \text{(D23)}$$

$$\sin 2\eta_{\mathrm{V}} = \frac{2\left|\frac{t_{sp}}{t_{ss}}\right|\sin\left(\arg\frac{t_{sp}}{t_{ss}}\right)}{1 + \left|\frac{t_{sp}}{t_{ss}}\right|^2}. \quad \text{(D24)}$$

In this work we rescale the calculated dielectric function in a slab model by the thickness of a monolayer material:

$$\varepsilon_{\alpha\alpha} = 1 + \frac{l}{d}(\tilde{\varepsilon}_{\alpha\alpha} - 1) \quad \text{(D25)}$$

and

$$\varepsilon_{\alpha\beta} = \frac{l}{d}\tilde{\varepsilon}_{\alpha\beta}, \quad \text{(D26)}$$

where l and d are thicknesses of the slab model along the out-of-plane direction and monolayer material, and $\tilde{\varepsilon}_{\alpha\alpha}$ and $\tilde{\varepsilon}_{\alpha\beta}$ are calculated dielectric functions in the BERKELEYGW package.

$\tilde{\varepsilon}_{\alpha\alpha}$ and $\tilde{\varepsilon}_{\alpha\beta}$ can be expressed as follows:

$$\mathrm{Im}[\varepsilon_{\alpha\alpha}(\omega)] = \frac{\pi\hbar^2}{\varepsilon_0 N_k V}\sum_S \frac{1}{\Omega_S^2}\left|\langle 0|\hat{j}_p^{\alpha}|S\rangle\right|^2[\delta(\hbar\omega - \Omega_S)], \quad \text{(D27)}$$

$$\mathrm{Re}[\varepsilon_{\alpha\alpha}(\omega)] = -\frac{\hbar^2}{\varepsilon_0 N_k V}\sum_S \frac{1}{\Omega_S^2}\left|\langle 0|\hat{j}_p^{\alpha}|S\rangle\right|^2\left[\frac{1}{\hbar\omega - \Omega_S}\right], \quad \text{(D28)}$$

and

$$\mathrm{Im}[\varepsilon_{\alpha\beta}(\omega)] = \frac{i\hbar^2}{\varepsilon_0 N_k V}\sum_S \frac{1}{\Omega_S^2}\left[\frac{\langle 0|\hat{j}_p^{\alpha}|S\rangle\langle S|\hat{j}_p^{\beta}|0\rangle}{\hbar\omega - \Omega_S}\right], \quad \text{(D29)}$$

$$\mathrm{Re}[\varepsilon_{\alpha\beta}(\omega)] = \frac{i\pi\hbar^2}{\varepsilon_0 N_k V}\sum_S \frac{1}{\Omega_S^2}\left[\langle 0|\hat{j}_p^{\alpha}|S\rangle\langle S|\hat{j}_p^{\beta}|0\rangle\delta(\hbar\omega - \Omega_S)\right], \quad \text{(D30)}$$

where N_k is the number of k points, V is the volume of a unit cell, $\hat{j}_p = -e\hat{v}$, and $\langle 0|\hat{j}_p^{\alpha}|S\rangle = \sum_{cvk} A_{cvk}^S\langle vk|\hat{j}_p^{\alpha}|ck\rangle$.
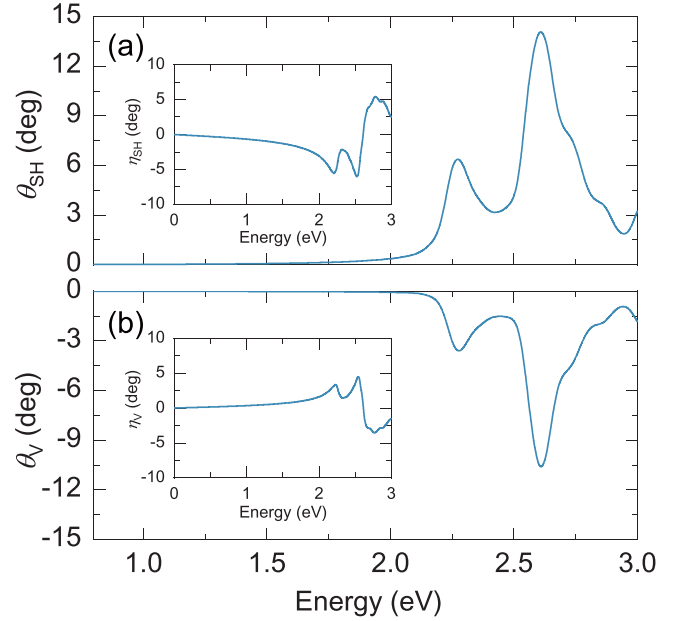
FIG. 15. Rotation angles of (a) reflected and (b) transmitted light in CrSBr monolayer without the inclusion of electron-hole interactions. Insets are the corresponding ellipticities.

APPENDIX E: CALCULATIONS OF SH AND VOIGT EFFECTS IN CRSBR

In Fig. 15 we show the calculated results without the consideration of electron-hole interaction, i.e., under independent particle approximation. In Fig. 16 we compare the results with and without the inclusion of off-diagonal components of dielectric function from BSE.

FIG. 16. Comparison of rotation angles for both (a) reflected and (b) transmitted lights in CrSBr monolayer between the situations with and without the inclusion of off-diagonal component ε_{xz}.

FIG. 17. Anisotropic optical absorbance in CrSBr monolayer with spin orientation along x axis for the electric polarization along x (a) and y (b) directions, respectively. (c) Exciton spectrum.

APPENDIX F: ABSORBANCE AND EXCITON SPECTRUM WITH SPIN ORIENTATION ALONG X AND Z AXIS

In Figs. 17 and 18 we show the anisotropic optical absorbance and exciton spectrum in CrSBr monolayer for states

FIG. 18. Anisotropic optical absorbance in CrSBr monolayer with spin orientation along z for the electric polarization along x (a) and y (b) directions, respectively. (c) Exciton spectrum.
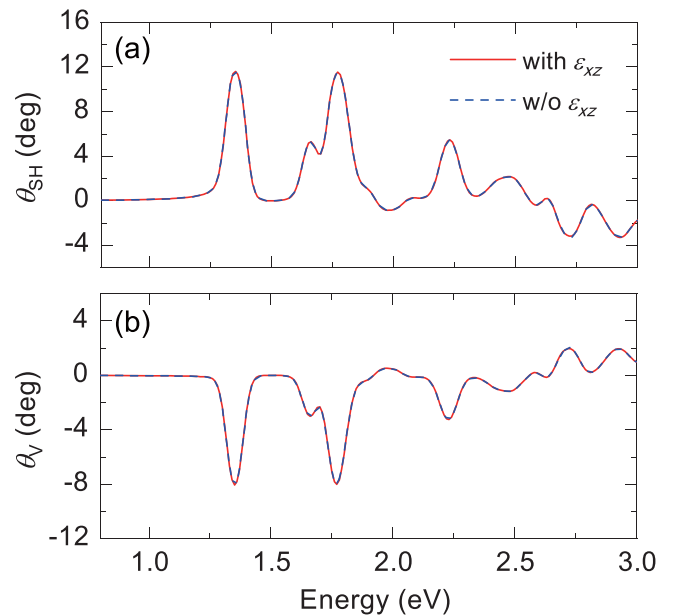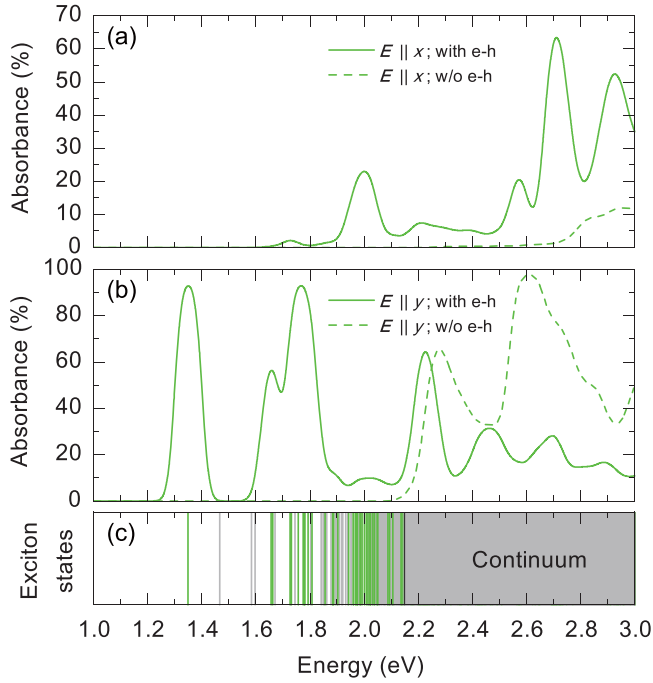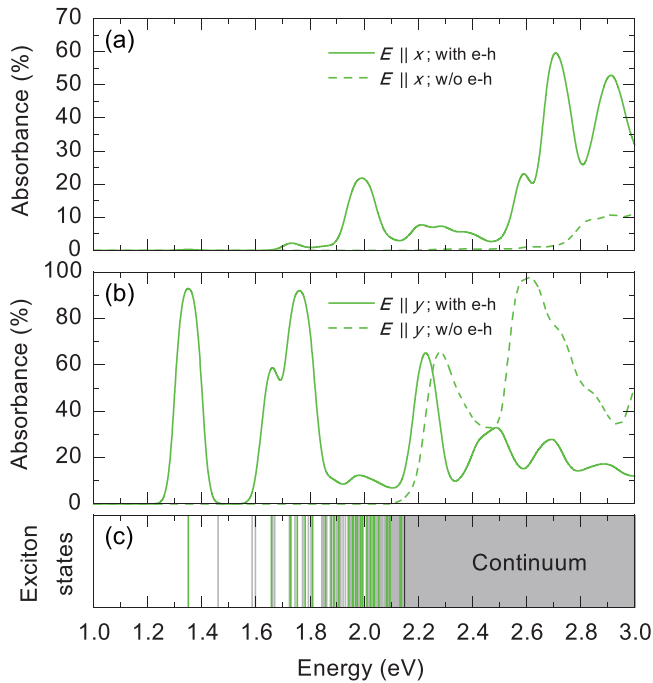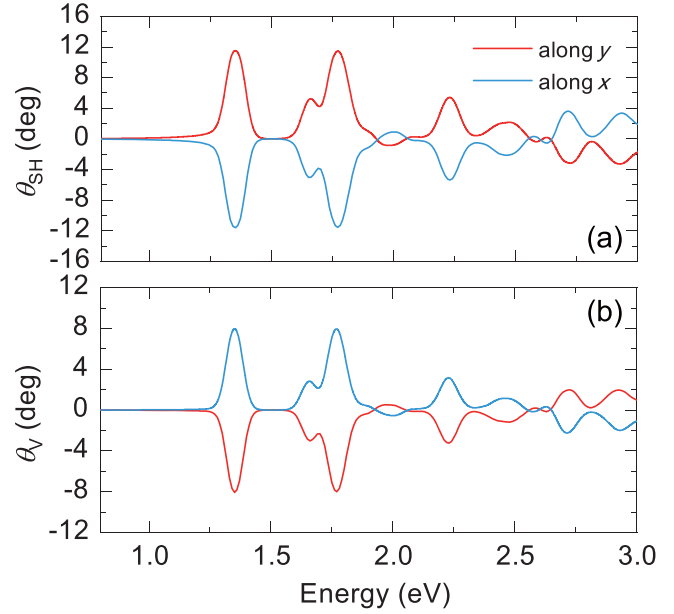

FIG. 19. Rotation angles of (a) reflected and (b) transmitted light in CrSBr monolayer for states with spin orientation along x (blue) and y (red) axis considering electron-hole interactions.

with spin orientation along the x axis and z axis, respectively. The optical absorbance and exciton spectrum for the state with spin orientation along the x axis are similar to those for the state with spin orientation along the z axis.

APPENDIX G: COMPARISON OF ROTATION ANGLES OF SH AND VOIGT EFFECTS FOR THE STATES WITH SPIN ORIENTATION ALONG X AND Y AXIS

In Fig. 19 we compare rotation angles for states with spin orientation along the x and y axis. It is obvious that rotation angles for the state with spin orientation along the x axis are nearly unchanged compared with those for the state with spin orientation along the y axis.

APPENDIX H: CALCULATIONS OF KERR AND FARADAY EFFECTS IN CRSBR WITH OUT-OF-PLANE MAGNETIZATION

In 2D magnets, the in-plane spin orientation could be tuned to the out-of-plane direction by an external perpendicular magnetic field. As shown in Fig. 20, here we consider the out-of-plane magnetization along the z axis ($\boldsymbol{B} = B\hat{\boldsymbol{e}}_z$). For an isotropic system the dielectric tensor is expressed as

$$\boldsymbol{\varepsilon}(\omega, \boldsymbol{B}) = \begin{pmatrix} \varepsilon_{xx}(\omega, \boldsymbol{B}) & \varepsilon_{xy}(\omega, \boldsymbol{B}) & 0 \\ -\varepsilon_{xy}(\omega, \boldsymbol{B}) & \varepsilon_{xx}(\omega, \boldsymbol{B}) & 0 \\ 0 & 0 & \varepsilon_{zz}(\omega, \boldsymbol{B}) \end{pmatrix}. \quad \text{(H1)}$$

The Fresnel equation for the propagation of an electromagnetic wave is given by

$$[n^2 \boldsymbol{I} - \boldsymbol{\varepsilon} - \boldsymbol{n} : \boldsymbol{n}] \cdot \boldsymbol{E} = 0. \quad \text{(H2)}$$
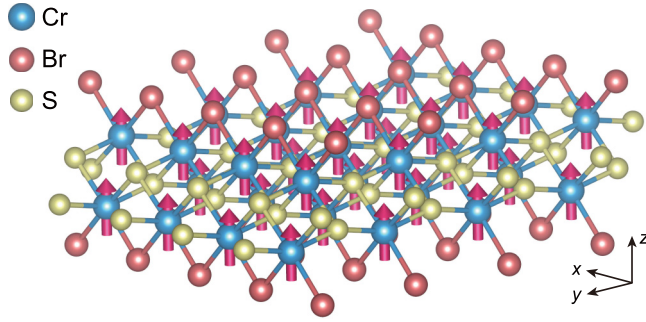
FIG. 20. Illustration of crystal structure of 2D magnet CrSBr monolayer with out-of-plane magnetization.

For normal incidence, the complex refractory index **n** is

$$\boldsymbol{n} = \frac{c\boldsymbol{k}}{\omega} = \frac{ck}{\omega}\hat{\boldsymbol{e}}_z. \tag{H3}$$

By solving the above Fresnel equations, we get the normal modes as the σ^+ and σ^- for circularly polarized plane waves, with distinct refractive indices:

$$n_\pm^2(\omega, B\hat{\boldsymbol{e}}_z) = \varepsilon_{xx}(\omega, B\hat{\boldsymbol{e}}_z) \pm i\varepsilon_{xy}(\omega, B\hat{\boldsymbol{e}}_z). \tag{H4}$$

For an anisotropic system, the distinct refractive indices are

$$n_\pm^2(\omega, B\hat{\boldsymbol{e}}_z) = \varepsilon_0(\omega, B\hat{\boldsymbol{e}}_z) \pm i\varepsilon_{xy}(\omega, B\hat{\boldsymbol{e}}_z), \tag{H5}$$

$$\varepsilon_0(\omega, B\hat{\boldsymbol{e}}_z) = \frac{\varepsilon_{xx}(\omega, B\hat{\boldsymbol{e}}_z) + \varepsilon_{yy}(\omega, B\hat{\boldsymbol{e}}_z)}{2}. \tag{H6}$$

To mathematically describe how an electromagnetic wave interacts with such stratified and anisotropic media, we adopt a 4×4 formalism involving the in-plane components of both electric (E_x, E_y) and magnetic fields (B_x, B_y). We consider a monolayer material magnetized along the $+z$ direction, and the second layer is vacuum. Within each layer ($l = 0, 1, 2$), we choose the four eigenmodes of light as follows: $\hat{\boldsymbol{e}}_1^{(l)} = \hat{\boldsymbol{e}}_2^{(l)} = \hat{\boldsymbol{e}}_+$, $\hat{\boldsymbol{e}}_3^{(l)} = \hat{\boldsymbol{e}}_4^{(l)} = \hat{\boldsymbol{e}}_-$, with the corresponding refractive indices: $n_1^{(l)} = -n_2^{(l)} = n_+^{(l)}$, $n_3^{(l)} = -n_4^{(l)} = n_-^{(l)}$. The electric and magnetic fields of light in the first and second layers are given by

$$\boldsymbol{E}^{(l)} = \sum_{j=1}^4 E_{0j}^{(l)} \hat{\boldsymbol{e}}_j^{(l)} \exp\left\{i\left[k_j^{(l)}(z - z_{l-1}) - \omega t\right]\right\} \tag{H7}$$

and

$$c\boldsymbol{B}^{(l)} = \sum_{j=1}^4 E_{0j}^{(l)} \boldsymbol{b}_j^{(l)} \exp\left\{i\left[k_j^{(l)}(z - z_{l-1}) - \omega t\right]\right\}, \tag{H8}$$

with $\boldsymbol{b}_j^{(l)} = n_j^{(l)}\hat{\boldsymbol{e}}_z \times \hat{\boldsymbol{e}}_j^{(l)}$. The electric and magnetic fields of light in the zeroth layer are given by

$$\boldsymbol{E}^{(0)} = \sum_{j=1}^4 E_{0j}^{(0)} \hat{\boldsymbol{e}}_j^{(0)} \exp\left\{i\left[k_j^{(0)}(z - z_0) - \omega t\right]\right\} \tag{H9}$$

and

$$c\boldsymbol{B}^{(0)} = \sum_{j=1}^4 E_{0j}^{(0)} \boldsymbol{b}_j^{(0)} \exp\left\{i\left[k_j^{(0)}(z - z_0) - \omega t\right]\right\}. \tag{H10}$$

The requirement of the continuity of the tangential field components at the interfaces connects the field amplitudes $E_{0j}^{(l)}$ between two neighboring layers. The dynamical matrix within each layer is given by a block-diagonal form:

$$\boldsymbol{D}^{(l)} = \begin{pmatrix} \hat{\boldsymbol{e}}_1^{(l)} \cdot \hat{\boldsymbol{e}}_+^* & \hat{\boldsymbol{e}}_2^{(l)} \cdot \hat{\boldsymbol{e}}_+^* & \hat{\boldsymbol{e}}_3^{(l)} \cdot \hat{\boldsymbol{e}}_+^* & \hat{\boldsymbol{e}}_4^{(l)} \cdot \hat{\boldsymbol{e}}_+^* \\ \hat{\boldsymbol{b}}_1^{(l)} \cdot \hat{\boldsymbol{e}}_+^* & \hat{\boldsymbol{b}}_2^{(l)} \cdot \hat{\boldsymbol{e}}_+^* & \hat{\boldsymbol{b}}_3^{(l)} \cdot \hat{\boldsymbol{e}}_+^* & \hat{\boldsymbol{b}}_4^{(l)} \cdot \hat{\boldsymbol{e}}_+^* \\ \hat{\boldsymbol{e}}_1^{(l)} \cdot \hat{\boldsymbol{e}}_-^* & \hat{\boldsymbol{e}}_2^{(l)} \cdot \hat{\boldsymbol{e}}_-^* & \hat{\boldsymbol{e}}_3^{(l)} \cdot \hat{\boldsymbol{e}}_-^* & \hat{\boldsymbol{e}}_4^{(l)} \cdot \hat{\boldsymbol{e}}_-^* \\ \hat{\boldsymbol{b}}_1^{(l)} \cdot \hat{\boldsymbol{e}}_-^* & \hat{\boldsymbol{b}}_2^{(l)} \cdot \hat{\boldsymbol{e}}_-^* & \hat{\boldsymbol{b}}_3^{(l)} \cdot \hat{\boldsymbol{e}}_-^* & \hat{\boldsymbol{b}}_4^{(l)} \cdot \hat{\boldsymbol{e}}_-^* \end{pmatrix}$$

$$= \begin{pmatrix} 1 & 1 & 0 & 0 \\ -in_+^{(l)} & in_+^{(l)} & 0 & 0 \\ 0 & 0 & 1 & 1 \\ 0 & 0 & in_-^{(l)} & -in_-^{(l)} \end{pmatrix}. \tag{H11}$$

The propagation matrix is defined as a diagonal matrix:

$$\boldsymbol{P}^{(1)} = \begin{pmatrix} e^{i\delta_+} & 0 & 0 & 0 \\ 0 & e^{-i\delta_+} & 0 & 0 \\ 0 & 0 & e^{i\delta_-} & 0 \\ 0 & 0 & 0 & e^{-i\delta_-} \end{pmatrix}, \tag{H12}$$

where $\delta_+ = \frac{\omega}{c}n_+$, $\delta_- = \frac{\omega}{c}n_-$, and d is the thickness of layer 1, i.e., monolayer CrSBr.

In this two-interface setup, $\boldsymbol{E}_0^{(0)}$ and $\boldsymbol{E}_0^{(2)}$ are related by the transfer matrix $\boldsymbol{M}_c$ in the basis of linearly polarized lights:

$$\boldsymbol{E}_0^{(2)} = \boldsymbol{M}_c \boldsymbol{E}_0^{(0)} = [\boldsymbol{D}^{(2)}]^{-1}\boldsymbol{D}^{(1)}\boldsymbol{P}^{(1)}[\boldsymbol{D}^{(1)}]^{-1}\boldsymbol{D}^{(0)}\boldsymbol{E}_0^{(0)}. \tag{H13}$$

$\boldsymbol{M}_c$ has a simple block-diagonal form:

$$\boldsymbol{M}_c = \begin{pmatrix} \boldsymbol{M}_+ & 0 \\ 0 & \boldsymbol{M}_- \end{pmatrix}, \tag{H14}$$

$$\boldsymbol{M}_+ = \frac{1}{t_{21}^+ t_{10}^+}\begin{pmatrix} e^{i\delta_+} + e^{-i\delta_+}r_{21}^+ r_{10}^+ & e^{i\delta_+}r_{10}^+ + e^{-i\delta_+}r_{21}^+ \\ e^{i\delta_+}r_{21}^+ + e^{-i\delta_+}r_{10}^+ & e^{i\delta_+}r_{21}^+ r_{10}^+ + e^{-i\delta_+} \end{pmatrix}, \tag{H15}$$

where r_{mn} and t_{mn} are the Fresnel coefficients of the interface from the mth layer to the nth layer, and $\boldsymbol{M}_-$ has the same form. In the left and right layers we adopt a basis transformation from the circularly polarized light ($\hat{\boldsymbol{e}}_+, \hat{\boldsymbol{e}}_-$) with $\hat{\boldsymbol{e}}_+ = -\frac{1}{\sqrt{2}}(\hat{\boldsymbol{e}}_x + i\hat{\boldsymbol{e}}_y)$ and $\hat{\boldsymbol{e}}_- = \frac{1}{\sqrt{2}}(\hat{\boldsymbol{e}}_x - i\hat{\boldsymbol{e}}_y)$ to the light ($\hat{\boldsymbol{e}}_x, \hat{\boldsymbol{e}}_y$). $\hat{\boldsymbol{e}}_1^{(l)} = \hat{\boldsymbol{e}}_2^{(l)} = \hat{\boldsymbol{e}}_x$, $\hat{\boldsymbol{e}}_3^{(l)} = \hat{\boldsymbol{e}}_4^{(l)} = \hat{\boldsymbol{e}}_y$, and $n_1^{(l)} = -n_2^{(l)} = n_3^{(l)} = -n_4^{(l)} = n^{(l)}$, for $l = 0, 2$. This new basis of linearly polarized plane waves is denoted as $\{x \rightarrow, x \leftarrow, y \rightarrow, y \leftarrow\}$. In this basis of linearly polarized lights, the electric field amplitudes in the left and right layer are related by transfer matrix $\boldsymbol{M}$:

$$\begin{pmatrix} E_{0x\rightarrow}^{(2)} \\ E_{0x\leftarrow}^{(2)} \\ E_{0y\rightarrow}^{(2)} \\ E_{0y\leftarrow}^{(2)} \end{pmatrix} = \boldsymbol{M} \begin{pmatrix} E_{0x\rightarrow}^{(0)} \\ E_{0x\leftarrow}^{(0)} \\ E_{0y\rightarrow}^{(0)} \\ E_{0y\leftarrow}^{(0)} \end{pmatrix}, \tag{H16}$$

$$\boldsymbol{M} = \frac{1}{2}\begin{pmatrix} \boldsymbol{M}_+ + \boldsymbol{M}_- & -i(\boldsymbol{M}_+ - \boldsymbol{M}_-) \\ i(\boldsymbol{M}_+ - \boldsymbol{M}_-) & \boldsymbol{M}_+ + \boldsymbol{M}_- \end{pmatrix}. \tag{H17}$$

Because the electric field of incident light is along the direction of magnetization ($+z$), $E_{0y\leftarrow}^{(2)} = 0$. In addition, there are no reflecting lights from the *zero*th medium (semi-infinite substrate) to CrSBr, which means $E_{0x\rightarrow}^{(0)} = E_{0y\rightarrow}^{(0)} = 0$. With these two conditions, by calculating Eq. (G16) we can get

$$t_{ss} \equiv \frac{E_{0x\leftarrow}^{(0)}}{E_{0x\leftarrow}^{(2)}} = \frac{\boldsymbol{M}_{44}}{\boldsymbol{M}_{22}\boldsymbol{M}_{44} - \boldsymbol{M}_{24}\boldsymbol{M}_{42}}, \tag{H18}$$

$$t_{sp} \equiv \frac{E_{0y\leftarrow}^{(0)}}{E_{0x\leftarrow}^{(2)}} = \frac{-\boldsymbol{M}_{42}}{\boldsymbol{M}_{22}\boldsymbol{M}_{44} - \boldsymbol{M}_{24}\boldsymbol{M}_{42}}, \tag{H19}$$

$$r_{ss} \equiv \frac{E_{0x\rightarrow}^{(0)}}{E_{0x\leftarrow}^{(2)}} = \frac{\boldsymbol{M}_{12}\boldsymbol{M}_{44} - \boldsymbol{M}_{14}\boldsymbol{M}_{42}}{\boldsymbol{M}_{22}\boldsymbol{M}_{44} - \boldsymbol{M}_{24}\boldsymbol{M}_{42}}, \tag{H20}$$

$$r_{sp} \equiv \frac{E_{0y\rightarrow}^{(0)}}{E_{0x\leftarrow}^{(2)}} = \frac{\boldsymbol{M}_{32}\boldsymbol{M}_{44} - \boldsymbol{M}_{34}\boldsymbol{M}_{42}}{\boldsymbol{M}_{22}\boldsymbol{M}_{44} - \boldsymbol{M}_{24}\boldsymbol{M}_{42}}. \tag{H21}$$

The Kerr signals for the reflected (right-moving) electric field $E_{\rightarrow}^{(2)} = E_{0x\rightarrow}^{(2)}\hat{\boldsymbol{e}}_x + E_{0y\rightarrow}^{(2)}\hat{\boldsymbol{e}}_y$ are expressed as

$$\tan 2\theta_{\mathrm{K}} = \frac{2\left|\frac{r_{sp}}{r_{ss}}\right|\cos\left(\arg\frac{r_{sp}}{r_{ss}}\right)}{1 - \left|\frac{r_{sp}}{r_{ss}}\right|^2}, \tag{H22}$$

$$\sin 2\eta_{\mathrm{K}} = \frac{2\left|\frac{r_{sp}}{r_{ss}}\right|\sin\left(\arg\frac{r_{sp}}{r_{ss}}\right)}{1 + \left|\frac{r_{sp}}{r_{ss}}\right|^2}. \tag{H23}$$

Similarly, the Faraday signals for the transmitted (left-moving) electric field $E_{\leftarrow}^{(0)} = E_{0x\leftarrow}^{(0)}\hat{\boldsymbol{e}}_x + E_{0y\leftarrow}^{(0)}\hat{\boldsymbol{e}}_y$ are expressed as

$$\tan 2\theta_{\mathrm{F}} = \frac{2\left|\frac{t_{sp}}{t_{ss}}\right|\cos\left(\arg\frac{t_{sp}}{t_{ss}}\right)}{1 - \left|\frac{t_{sp}}{t_{ss}}\right|^2}, \tag{H24}$$

FIG. 21. Magneto-optical Kerr and Faraday effects. Rotation angles of (a) reflected and (b) transmitted light in CrSBr monolayer for the state with spin orientation along the z axis considering electron-hole interactions. Insets are the corresponding ellipticities.
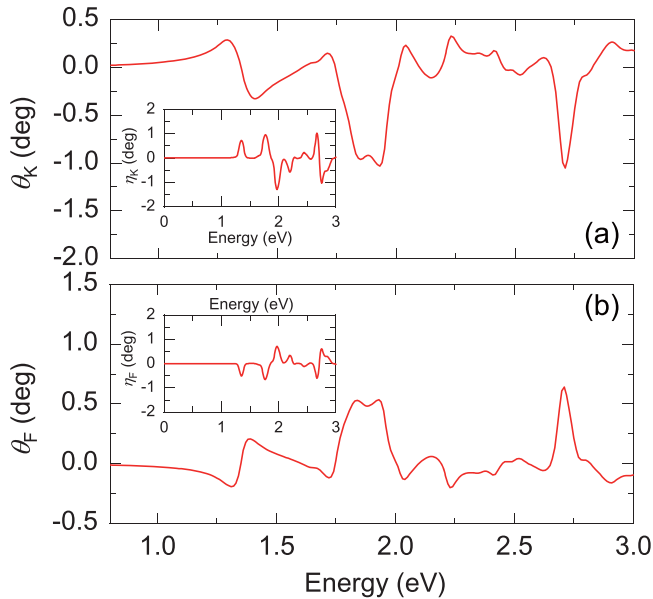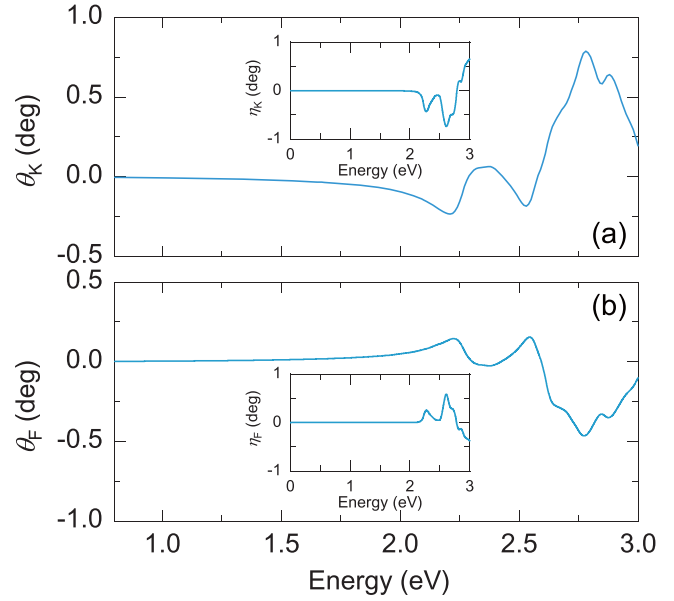

FIG. 22. Magneto-optical Kerr and Faraday effects. Rotation angles of (a) reflected and (b) transmitted light in CrSBr monolayer for the state with spin orientation along z axis without the inclusion of electron-hole interactions. Insets are the corresponding ellipticities.

$$\sin 2\eta_{\mathrm{F}} = \frac{2\left|\frac{t_{sp}}{t_{ss}}\right|\sin\left(\arg\frac{t_{sp}}{t_{ss}}\right)}{1 + \left|\frac{t_{sp}}{t_{ss}}\right|^2}. \tag{H25}$$
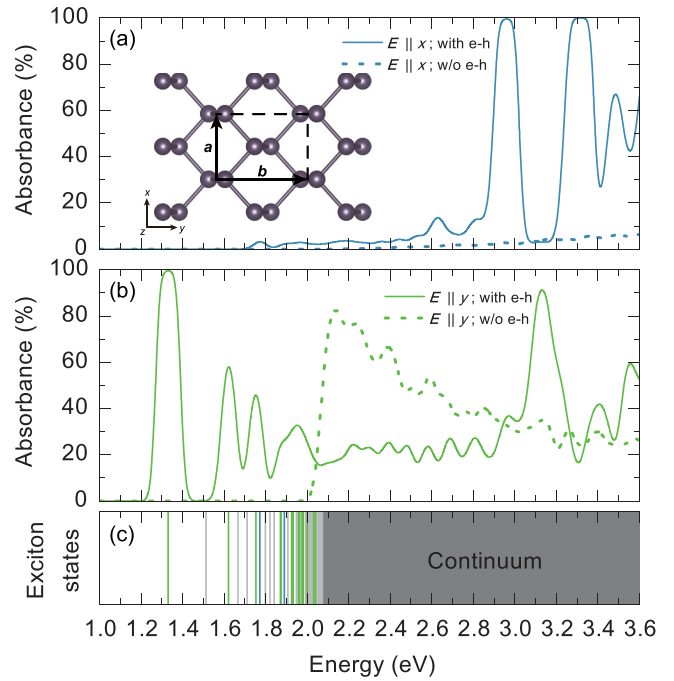

FIG. 23. Anisotropic optical absorbance in black phosphorene monolayer for the electric polarization along x (a) and y (b) directions, respectively. (c) Exciton spectrum. Both optical spectra with and without the consideration of electron-hole interaction are presented. Inset of (a) is the crystal structure of black phosphorene, and the gray lines are for dark excitons.
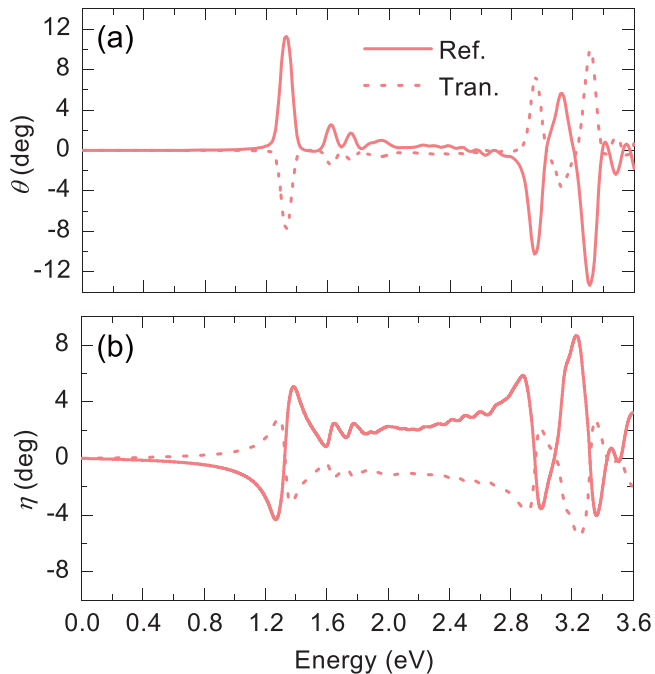
FIG. 24. Rotation angles (a) and ellipticities (b) in black phosphorene.

Based on the above derivation, in Fig. 21 we show rotation angles and ellipticities of Kerr and Faraday effects considering

electron-hole interaction. The maximal rotation angles of Kerr and Faraday effects are $1.1°$ and $0.6°$, respectively, which are larger than $0.9°$ and $0.3°$ in CrI_3 [9] and $0.3°$ and $0.2°$ in $CrBr_3$ [10]. Compared with Fig. 22, both the amplitude and the position of the spectrum are modified significantly for excitonic effect. This verifies the fact that it is the excitonic effect that enhances the Kerr and Faraday effects in the CrSBr monolayer.

APPENDIX I: G_0W_0-BSE CALCULATIONS OF OPTICAL PROPERTIES IN BLACK PHOSPHORENE

In Fig. 23 we show the anisotropic optical absorption spectrum and exciton states (within the G_0W_0-BSE framework) for black phosphorene. We use the norm-conserving PBE pseudopotentials with a plane-wave cutoff of 80 Ry. For the G_0W_0 part we use a coarse k grid of $18×12×1\,500$ empty bands (five valence bands), and a dielectric cutoff of 10 Ry. For the BSE part, a fine k grid of $72×48×1$ is used. A Gaussian smearing with a broadening constant of 30 meV is used in optical absorption spectrum. The number of bands for optical transitions is four for both valence and conduction bands, which is sufficient to cover the span of the visible light. The lattice constants are 3.303 Å for a and 4.625 Å for b. In Fig. 24 we show the linear dichroism for both reflected and transmitted light with rotation angle and ellipticity.

[1] F. Xia, H. Wang, D. Xiao, M. Dubey, and A. Ramasubramaniam, Two-dimensional material nanophotonics, Nat. Photon. **8**, 899 (2014).

[2] K. F. Mak and J. Shan, Photonics and optoelectronics of 2D semiconductor transition metal dichalcogenides, Nat. Photon. **10**, 216 (2016).

[3] Z. Sun, A. Martinez, and F. Wang, Optical modulators with 2D layered materials, Nat. Photon. **10**, 227 (2016).

[4] N. P. Wilson, W. Yao, J. Shan, and X. Xu, Excitons and emergent quantum phenomena in stacked 2D semiconductors, Nature (London) **599**, 383 (2021).

[5] C. Gong, L. Li, Z. Li, H. Ji, A. Stern, Y. Xia, T. Cao, W. Bao, C. Wang, Y. Wang, Z. Q. Qiu, R. J. Cava, S. G. Louie, J. Xia, and X. Zhang, Discovery of intrinsic ferromagnetism in two-dimensional van der Waals crystals, Nature (London) **546**, 265 (2017).

[6] B. Huang, G. Clark, E. Navarro-Moratalla, D. R. Klein, R. Cheng, K. L. Seyler, D. Zhong, E. Schmidgall, M. A. McGuire, D. H. Cobden, W. Yao, D. Xiao, P. Jarillo-Herrero, and X. Xu, Layer-dependent ferromagnetism in a van der Waals crystal down to the monolayer limit, Nature (London) **546**, 270 (2017).

[7] Y. Fang, S. Wu, Z. Z. Zhu, and G. Y. Guo, Large magneto-optical effects and magnetic anisotropy energy in two-dimensional $Cr_2Ge_2Te_6$, Phys. Rev. B **98**, 125416 (2018).

[8] V. K. Gudelli and G. Y. Guo, Magnetism and magneto-optical effects in bulk and few-layer CrI_3: A theoretical GGA+U study, New J. Phys. **21**, 053012 (2019).

[9] M. Wu, Z. Li, T. Cao, and S. G. Louie, Physical origin of giant excitonic and magneto-optical responses in two-dimensional ferromagnetic insulators, Nat. Commun. **10**, 2371 (2019).

[10] M. Wu, Z. Li, and S. G. Louie, Optical and magneto-optical properties of ferromagnetic monolayer $CrBr_3$: A first-principles GW and GW plus Bethe-Salpeter equation study, Phys. Rev. Mater. **6**, 014008 (2022).

[11] N. Mounet, N. Mounet, M. Gibertini, P. Schwaller, D. Campi, A. Merkys, A. Marrazzo, T. Sohier, I. E. Castelli, A. Cepellotti, G. Pizzi, and N. Marzari, Two-dimensional materials from high-throughput computational exfoliation of experimentally known compounds, Nat. Nanotechnol. **13**, 246 (2018).

[12] N. P. Wilson, K. Lee, J. Cenker, K. Xie, A. H. Dismukes, E. J. Telford, J. Fonseca, S. Sivakumar, C. Dean, T. Cao, X. Roy, X. Xu, and X. Zhu, Interlayer electronic coupling on demand in a 2D magnetic semiconductor, Nat. Mater. **20**, 1657 (2021).

[13] Y. J. Bae, J. Wang, A. Scheie, J. Xu, D. G. Chica, G. M. Diederich, J. Cenker, M. E. Ziebel, Y. Bai, H. Ren, C. R. Dean, M. Delor, X. Xu, X. Roy, A. D. Kent, and X. Zhu, Exciton-coupled coherent magnons in a 2D semiconductor, Nature (London) **609**, 282 (2022).

[14] N. Tesařová, T. Ostatnický, V. Novák, K. Olejník, J. Šubrt, H. Reichlová, C. T. Ellis, A. Mukherjee, J. Lee, G. M. Sipahi, J. Sinova, J. Hamrle, T. Jungwirth, P. Němec, J. Černe, and K. Výborný, Systematic study of magnetic linear dichroism and birefringence in (Ga, Mn)As, Phys. Rev. B **89**, 085203 (2014).

[15] X. Yang, P. Yang, X. Zhou, W. Feng, and Y. Yao, First- and second-order magneto-optical effects and intrinsically anomalous transport in the two-dimensional van der Waals layered magnets Cr*XY* (*X* = S, Se, Te; *Y* = Cl, Br, I), Phys. Rev. B **106**, 054408 (2022).

[16] M. L. Cohen and S. G. Louie, *Fundamentals of Condensed Matter Physics* (Cambridge University Press, Cambridge, England, 2016).

[17] L. V. Keldysh, Coulomb interaction in thin semiconductor and semimetal films, JETP Lett. **29**, 658 (1979).

[18] P. Cudazzo, I. V. Tokatly, and A. Rubio, Dielectric screening in two-dimensional insulators: Implications for excitonic and impurity states in graphane, Phys. Rev. B **84**, 085406 (2011).

[19] T. C. Berkelbach, M. S. Hybertsen, and D. R. Reichman, Theory of neutral and charged excitons in monolayer transition metal dichalcogenides, Phys. Rev. B **88**, 045318 (2013).

[20] A. S. Rodin, A. Carvalho, and A. H. Castro Neto, Excitons in anisotropic two-dimensional semiconducting crystals, Phys. Rev. B **90**, 075429 (2014).

[21] T. Olsen, S. Latini, F. Rasmussen, and K. S. Thygesen, Simple Screened Hydrogen Model of Excitons in Two-Dimensional Materials, Phys. Rev. Lett. **116**, 056401 (2016).

[22] G. Onida, L. Reining, and A. Rubio, Electronic excitations: Density-functional versus many-body Green's function approaches, Rev. Mod. Phys. **74**, 601 (2002).

[23] P. Giannozzi, S. Baroni, N. Bonini, M. Calandra, R. Car, C. Cavazzoni, D. Ceresoli, G. L. Chiarotti, M. Cococcioni, I. Dabo, A. D. Corso, S. de Gironcoli, S. Fabris, G. Fratesi, R. Gebauer, U. Gerstmann, C. Gougoussis, A. Kokalj, M. Lazzeri, L. Martin-Samos *et al.*, QUANTUM ESPRESSO: A modular and open-source software project for quantum simulations of materials, J. Phys.: Condens. Matter **21**, 395502 (2009).

[24] J. P. Perdew, K. Burke, and M. Ernzerhof, Generalized Gradient Approximation Made Simple, Phys. Rev. Lett. **77**, 3865 (1996).

[25] D. R. Hamann, Optimized norm-conserving Vanderbilt pseudopotentials, Phys. Rev. B **88**, 085117 (2013).

[26] M. S. Hybertsen and S. G. Louie, Electron correlation in semiconductors and insulators: Band gaps and quasiparticle energies, Phys. Rev. B **34**, 5390 (1986).

[27] M. Rohlfing and S. G. Louie, Electron-hole excitations and optical spectra from first principles, Phys. Rev. B **62**, 4927 (2000).

[28] J. Deslippe, G. Samzonidze, D. A. Strubbe, M. Jain, M. L. Cohen, and S. G. Louie, BerkeleyGW: A massively parallel computer package for the calculation of the quasiparticle and optical properties of materials and nanostructures, Comput. Phys. Commun. **183**, 1269 (2012).

[29] B. A. Barker, J. Deslippe, J. Lischner, M. Jain, O. V. Yazyev, D. A. Strubbe, and S. G. Louie, Spinor GW/Bethe-Salpeter calculations in BerkeleyGW: Implementation, symmetries, benchmarking, and performance, Phys. Rev. B **106**, 115127 (2022).

[30] S. Ismail-Beigi, Truncation of periodic image interactions for confined systems, Phys. Rev. B **73**, 233103 (2006).

[31] B. C. Shih, Y. Xue, P. Zhang, M. L. Cohen, and S. G. Louie, Quasiparticle Band Gap of ZnO: High Accuracy from the Conventional G^0W^0 Approach, Phys. Rev. Lett. **105**, 146401 (2010).

[32] K. Xie, X. Li, and T. Cao, Theory and ab initio calculation of optically excited states-recent advances in 2D materials, Adv. Mater. **33**, 1904306 (2021).

[33] L. Yang, J. Deslippe, C. H. Park, M. L. Cohen, and S. G. Louie, Excitonic Effects on the Optical Response of Graphene and Bilayer Graphene, Phys. Rev. Lett. **103**, 186802 (2009).

[34] C. H. Park and S. G. Louie, Tunable excitons in biased bilayer graphene, Nano Lett. **10**, 426 (2010).

[35] L. Yang, First-principles study of the optical absorption spectra of electrically gated bilayer graphene, Phys. Rev. B **81**, 155445 (2010).

[36] L. Yang, Excitons in intrinsic and bilayer graphene, Phys. Rev. B **83**, 085405 (2011).

[37] Y. Liang and L. Yang, Quasiparticle energy and optical excitations of gated bilayer graphene, Phys. Rev. B **86**, 205423 (2012).

[38] Y. Liang, R. Soklaski, S. Huang, M. W. Graham, R. Havener, J. Park, and L. Yang, Strongly bound excitons in gapless two-dimensional structures, Phys. Rev. B **90**, 115418 (2014).

[39] T. Cao, M. Wu, and S. G. Louie, Unifying Optical Selection Rules for Excitons in Two Dimensions: Band Topology and Winding Numbers, Phys. Rev. Lett. **120**, 087402 (2018).

[40] S. Huang, Y. Liang, and L. Yang, Exciton spectra in two-dimensional graphene derivatives, Phys. Rev. B **88**, 075441 (2013).

[41] D. Y. Qiu, F. H. da Jornada, and S. G. Louie, Optical Spectrum of MoS$_2$: Many-Body Effects and Diversity of Exciton States, Phys. Rev. Lett. **111**, 216805 (2013).

[42] R. Soklaski, Y. Liang, and L. Yang, Temperature effect on optical spectra of monolayer molybdenum disulfide, Appl. Phys. Lett. **104**, 193110 (2014).

[43] D. Y. Qiu, T. Cao, and S. G. Louie, Nonanalyticity, Valley Quantum Phases, and Lightlike Exciton Dispersion in Monolayer Transition Metal Dichalcogenides: Theory and First-Principles Calculations, Phys. Rev. Lett. **115**, 176801 (2015).

[44] D. Y. Qiu, F. H. da Jornada, and S. G. Louie, Screening and many-body effects in two-dimensional crystals: Monolayer MoS$_2$, Phys. Rev. B **93**, 235435 (2016).

[45] W. Song and L. Yang, Quasiparticle band gaps and optical spectra of strained monolayer transition-metal dichalcogenides, Phys. Rev. B **96**, 235441 (2017).

[46] M. H. Naik and M. Jain, Origin of layer dependence in band structures of two-dimensional materials, Phys. Rev. B **95**, 165125 (2017).

[47] S. Gao, L. Yang, and C. D. Spataru, Interlayer coupling and gate-tunable excitons in transition metal dichalcogenide heterostructures, Nano Lett. **17**, 7809 (2017).

[48] M. H. Naik and M. Jain, Substrate screening effects on the quasiparticle band gap and defect charge transition levels in MoS$_2$, Phys. Rev. Mater. **2**, 084002 (2018).

[49] S. Refaely-Abramson, D. Y. Qiu, S. G. Louie, and J. B. Neaton, Defect-Induced Modification of Low-Lying Excitons and Valley Selectivity in Monolayer Transition Metal Dichalcogenides, Phys. Rev. Lett. **121**, 167402 (2018).

[50] X. Lu, X. Li, and L. Yang, Modulated interlayer exciton properties in a two-dimensional moiré crystal, Phys. Rev. B **100**, 155416 (2019).

[51] M. H. Naik, E. C. Regan, Z. Zhang, Y. H. Chan, Z. Li, D. Wang, Y. Yoon, C. S. Ong, W. Zhao, S. Zhao, M. I. B. Utama, B. Gao, X. Wei, M. Sayyad, K. Yumigeta, K. Watanabe, T. Taniguchi, S.

Tongay, F. H. da Jornada, F. Wang, and S. G. Louie, Intralayer charge-transfer moiré excitons in van der Waals superlattices, Nature (London) **609**, 52 (2022).

[52] V. Tran, R. Soklaski, Y. Liang, and L. Yang, Layer-controlled band gap and anisotropic excitons in few-layer black phosphorus, Phys. Rev. B **89**, 235319 (2014).

[53] V. Tran, R. Fei, and L. Yang, Quasiparticle energies, excitons, and optical spectra of few-layer black phosphorus, 2D Mater. **2**, 044014 (2015).

[54] D. Y. Qiu, F. H. da Jornada, and S. G. Louie, Environmental screening effects in 2D materials: Renormalization of the bandgap, electronic structure, and optical spectra of few-layer black phosphorus, Nano Lett. **17**, 4706 (2017).

[55] T. Cao, Z. Li, D. Y. Qiu, and S. G. Louie, Gate switchable transport and optical anisotropy in 90° twisted bilayer black phosphorus, Nano Lett. **16**, 5542 (2016).

[56] Y. Chen and S. Y. Quek, Tunable bright interlayer excitons in few-layer black phosphorus based van der Waals heterostructures, 2D Mater. **5**, 045031 (2018).

[57] J. Zhou, T. Y. Cai, and S. Ju, Unusual Strain Dependence of Quasiparticle Electronic Structure, Exciton, and Optical Properties in Blue Phosphorene, Phys. Rev. Appl. **15**, 024045 (2021).

[58] J. Zhou, T. Y. Cai, and S. Ju, Quasiparticle band structure, exciton, and optical properties of few-layer blue phosphorus, Phys. Rev. B **104**, 245401 (2021).

[59] J. Zhou, T. Y. Cai, and S. Ju, Anisotropic exciton excitations and optical properties of Hittorf's phosphorene, Phys. Rev. Res. **2**, 033288 (2020).

[60] J. Zhou, T. Y. Cai, and S. Ju, Giant Stark Effect in two-dimensional Hittorf's Phosphorene, Phys. Rev. Appl. **17**, 054047 (2022).

[61] G. Antonius, D. Y. Qiu, and S. G. Louie, Orbital symmetry and the optical response of single-layer MX monochalcogenides, Nano Lett. **18**, 1925 (2018).

[62] G. Shi and E. Kioupakis, Anisotropic spin transport and strong visible-light absorbance in few-layer SnSe and GeSe, Nano Lett. **15**, 6926 (2015).

[63] Y. H. Chan, D. Y. Qiu, F. H. da Jornada, and S. G. Louie, Giant exciton-enhanced shift currents and direct current conduction with subbandgap photo excitations produced by many-electron interactions, Proc. Natl. Acad. Sci. USA **118**, e1906938118 (2021).

[64] N. Sanders, D. Bayerl, G. Shi, K. A. Mengle, and E. Kioupakis, Electronic and optical properties of two-dimensional GaN from first-principles, Nano Lett. **17**, 7345 (2017).

[65] X. Blase, A. Rubio, S. G. Louie, and M. L. Cohen, Quasiparticle band structure of bulk hexagonal boron nitride and related systems, Phys. Rev. B **51**, 6868 (1995).

[66] K. A. Mengle and E. Kioupakis, Impact of the stacking sequence on the bandgap and luminescence properties of bulk, bilayer, and monolayer hexagonal boron nitride, APL Mater. **7**, 021106 (2019).

[67] F. Zhang, C. S. Ong, J. W. Ruan, M. Wu, X. Q. Shi, Z. K. Tang, and S. G. Louie, Intervalley Excitonic Hybridization, Optical Selection Rules, and Imperfect Circular Dichroism in Monolayer h-BN, Phys. Rev. Lett. **128**, 047402 (2022).

[68] L. Zhu and L. Yang, Quasiparticle energies and excitonic effects of chromium trichloride: From two dimensions to bulk, Phys. Rev. B **101**, 245401 (2020).

[69] K. Lee, A. H. Dismukes, E. J. Telford, R. A. Wiscons, J. Wang, X. Xu, C. Nuckolls, C. R. Dean, X. Roy, and X. Zhu, Magnetic order and symmetry in the 2D semiconductor CrSBr, Nano Lett. **21**, 3511 (2021).

[70] K. Yang, G. Wang, L. Liu, D. Lu, and H. Wu, Triaxial magnetic anisotropy in the two-dimensional ferromagnetic semiconductor CrSBr, Phys. Rev. B **104**, 144416 (2021).

[71] G. Pizzi, V. Vitale, R. Arita, S. Blügel, F. Freimuth, G. Géranton, M. Gibertini, D. Gresch, C. Johnson, T. Koretsune, J. Ibañez-Azpiroz, H. Lee, J. Lihm, D. Marchand, A. Marrazzo, Y. Mokrousov, J. I. Mustafa, Y. Nohara, Y. Nomura, L. Paulatto, S. Poncé, T. Ponweiser, J. Qiao, F. Thöle, S. S. Tsirkin *et al.*, Wannier90 as a community code: New features and applications, J. Phys.: Condens. Matter **32**, 165902 (2020).

[72] R. Schuster, J. Trinckauf, C. Habenicht, M. Knupfer, and B. Büchner, Anisotropic Particle-Hole Excitations in Black Phosphorus, Phys. Rev. Lett. **115**, 026404 (2015).

[73] X. Wang, A. M. Jones, K. L. Seyler, V. Tran, Y. Jia, H. Zhao, H. Wang, L. Yang, X. Xu, and F. Xia, Highly anisotropic and robust excitons in monolayer black phosphorus, Nat. Nanotechnol. **10**, 517 (2015).

[74] H. Yuan, X. Liu, F. Afshinmanesh, W. Li, G. Xu, J. Sun, B. Lian, A. G. Curto, G. Ye, Y. Hikita, Z. Shen, S. C. Zhang, X. Chen, M. Brongersma, H. Y. Hwang, and Y. Cui, Polarization-sensitive broadband photodetector using a black phosphorus vertical p-n junction, Nat. Nanotechnol. **10**, 707 (2015).

[75] L. Li, J. Kim, C. Jin, G. J. Ye, D. Y. Qiu, F. H. da Jornada, Z. Shi, L. Chen, Z. Zhang, F. Yang, K. Watanabe, T. Taniguchi, W. Ren, S. G. Louie, X. H. Chen, Y. Zhang, and F. Wang, Direct observation of the layer-dependent electronic structure in phosphorene, Nat. Nanotechnol. **12**, 21 (2017).

[76] C. D. Spataru, S. Ismail-Beigi, R. B. Capaz, and S. G. Louie, Theory and *Ab Initio* Calculation of Radiative Lifetime of Excitons in Semiconducting Carbon Nanotubes, Phys. Rev. Lett. **95**, 247402 (2005).

[77] M. Palummo, M. Bernardi, and J. C. Grossman, Exciton radiative lifetimes in two-dimensional transition metal dichalcogenides, Nano Lett. **15**, 2794 (2015).

[78] J. Yang, R. Xu, J. Pei, Y. W. Myint, F. Wang, Z. Wang, S. Zhang, Z. Yu, and Y. Lu, Optical tuning of exciton and trion emissions in monolayer phosphorene, Light Sci. Appl. **4**, e312 (2015).

[79] Q. Cui, J. He, Z. Bellus Matthew, M. Mirzokarimov, T. Hofmann, H.-Y. Chiu, M. Antonik, D. He, Y. Wang, and H. Zhao, Transient absorption measurements on anisotropic monolayer ReS$_2$, Small **11**, 5565 (2015).

[80] T. Korn, S. Heydrich, M. Hirmer, J. Schmutzler, and C. Schüller, Low-temperature photocarrier dynamics in monolayer MoS$_2$, Appl. Phys. Lett. **99**, 102109 (2011).

[81] D. Lagarde, L. Bouet, X. Marie, C. R. Zhu, B. L. Liu, T. Amand, P. H. Tan, and B. Urbaszek, Carrier and Polarization Dynamics in Monolayer MoS$_2$, Phys. Rev. Lett. **112**, 047401 (2014).

[82] H. Shi, R. Yan, S. Bertolazzi, J. Brivio, B. Gao, A. Kis, D. Jena, H. G. Xing, and L. Huang, Exciton dynamics in suspended monolayer and few-layer MoS$_2$ 2D crystals, ACS Nano **7**, 1072 (2013).

[83] C. Robert, D. Lagarde, F. Cadiz, G. Wang, B. Lassagne, T. Amand, A. Balocchi, P. Renucci, S. Tongay, B. Urbaszek,

and X. Marie, Exciton radiative lifetime in transition metal dichalcogenide monolayers, Phys. Rev. B **93**, 205423 (2016).

[84] N. Kumar, Q. Cui, F. Ceballos, D. He, Y. Wang, and H. Zhao, Exciton-exciton annihilation in MoSe$_2$ monolayers, Phys. Rev. B **89**, 125427 (2014).

[85] G. Wang, L. Bouet, D. Lagarde, M. Vidal, A. Balocchi, T. Amand, X. Marie, and B. Urbaszek, Valley dynamics probed through charged and neutral exciton emission in monolayer WSe$_2$, Phys. Rev. B **90**, 075413 (2014).

[86] S. Mouri, Y. Miyauchi, M. Toh, W. Zhao, G. Eda, and K. Matsuda, Nonlinear photoluminescence in atomically thin layered WSe$_2$ arising from diffusion-assisted exciton-exciton annihilation, Phys. Rev. B **90**, 155449 (2014).

[87] T. Langer, A. Chernikov, D. Kalincev, M. Gerhard, H. Bremers, U. Rossow, M. Koch, and A. Hangleiter, Room temperature excitonic recombination in GaInN/GaN quantum wells, Appl. Phys. Lett. **103**, 202106 (2013).

[88] AM 1.5 G solar spectrum from http://rredc.nrel.gov/solar/spectra/am1.5.